Article:
Heymsfield, A, Krämer, M, Wood, NB et al. (2017) Dependence of the Ice Water Content and Snowfall Rate on Temperature, Globally: Comparison of In-Situ Observations, Satellite Active Remote Sensing Retrievals and Global Climate Model Simulations. Journal of Applied Meteorology and Climatology, 56 (1). ISSN: 1558-8432

https://doi.org/10.1175/JAMC-D-16-0230.1

Dependence of the Ice Water Content and Snowfall Rate on Temperature, Globally: Comparison of in Situ Observations, Satellite Active Remote Sensing Retrievals, and Global Climate Model Simulations

ANDREW HEYMSFIELD,[a] MARTINA KRÄMER,[b] NORMAN B. WOOD,[c] ANDREW GETTELMAN,[a] PAUL R. FIELD,[d] AND GUOSHENG LIU[e]

[a] *National Center for Atmospheric Research,*[f] *Boulder, Colorado*
[b] *Forschungszentrum Juelich, Juelich, Germany*
[c] *Cooperative Institute for Meteorological Satellite Studies, University of Wisconsin–Madison, Madison, Wisconsin*
[d] *Met Office, Exeter, United Kingdom*
[e] *The Florida State University, Tallahassee, Florida*

(Manuscript received 24 June 2016, in final form 13 October 2016)

ABSTRACT

Cloud ice microphysical properties measured or estimated from in situ aircraft observations are compared with global climate models and satellite active remote sensor retrievals. Two large datasets, with direct measurements of the ice water content (IWC) and encompassing data from polar to tropical regions, are combined to yield a large database of in situ measurements. The intention of this study is to identify strengths and weaknesses of the various methods used to derive ice cloud microphysical properties. The in situ data are measured with total water hygrometers, condensed water probes, and particle spectrometers. Data from polar, midlatitude, and tropical locations are included. The satellite data are retrieved from *CloudSat*/*CALIPSO* [the *CloudSat* Ice Cloud Property Product (2C-ICE) and 2C-SNOW-PROFILE] and Global Precipitation Measurement (GPM) Level2A. Although the 2C-ICE retrieval is for IWC, a method to use the IWC to get snowfall rates S is developed. The GPM retrievals are for snowfall rate only. Model results are derived using the Community Atmosphere Model (CAM5) and the Met Office Unified Model [Global Atmosphere 7 (GA7)]. The retrievals and model results are related to the in situ observations using temperature and are partitioned by geographical region. Specific variables compared between the in situ observations, models, and retrievals are the IWC and S. Satellite-retrieved IWCs are reasonably close in value to the in situ observations, whereas the models' values are relatively low by comparison. Differences between the in situ IWCs and those from the other methods are compounded when S is considered, leading to model snowfall rates that are considerably lower than those derived from the in situ data. Anomalous trends with temperature are noted in some instances.

1. Introduction

Snowfall is a key component of the earth's water and energy cycle. Even in tropical regions, rain at the surface is often linked to snow aloft (Field and Heymsfield 2015). Snow not only modifies the temperature at the surface because of its albedo relative to land surfaces, but snow aloft modulates cloud dynamics and global circulation patterns (Waliser et al. 2011). Accurate representation of snowfall at the ground is one of the key challenges confronted by weather forecast and climate models, but this requires a good representation of the snowfall rate in the vertical column above the surface. The purpose of this study, therefore, is to evaluate how reliably ice mass (IWC) and ice mass flux/snowfall rate (S) are being derived by climate models and retrieved from spaceborne active remote sensors, by comparing, statistically, the IWC and S from these data sources with a large set of aircraft in situ microphysical data that span locations from the tropics to the Arctic.

Characterizing the vertical distribution of the ice microphysics globally has been difficult because of the absence, or limited coverage, of ground-based observing systems. Space-based microwave radiometer measurements can provide snowfall rates at the surface, but not their vertical distribution. This hurdle has been overcome to a large extent by satellite-based observations

[f] The National Center for Atmospheric Research is sponsored by the National Science Foundation.

Corresponding author e-mail: Andrew Heymsfield, heyms1@ucar.edu

DOI: 10.1175/JAMC-D-16-0230.1

from *CloudSat* and the Global Precipitation Measurement (GPM) mission.

CloudSat, with its 94-GHz Cloud Profiling Radar (CPR), was designed to measure the vertical structure of clouds from space; measurements from *CloudSat* also allow the retrieval of precipitation data aloft as well as just above the surface, and the global database can be used to evaluate and improve weather forecast and climate models (Stephens et al. 2002). The CPR on board *CloudSat* is proving to be a useful tool for mapping the vertical distribution of IWC and S globally, in part because of its high sensitivity to light precipitation and its ability to provide near-global data (Liu 2008; Wood et al. 2014). The radar-only (2B-CWC-RO) and radar-optical depth (2B-CWC-RVOD) products are the standard products used to retrieve the IWC. The IWC from the *CloudSat* Ice Cloud Property Product (2C-ICE; Deng et al. 2015) is intended to incorporate additional observations (i.e., *CALIPSO*) that improve the sensitivity to small ice particles relative to radar-only retrievals. The product 2C-SNOW-PROFILE (hereinafter 2C-SP; Wood et al. 2013) is intended to retrieve snowfall rate. Although the *CloudSat* radar is about an order of magnitude more sensitive to very light precipitation than any other existing space-based radar (Skofronick-Jackson et al. 2013), *CloudSat* reflectivities attenuate in deep, higher-rate snowfall events (Cao et al. 2014).

The GPM, launched in 2014, is a constellation-based satellite mission specifically designed to provide observations of rainfall and snowfall from space in order to improve the understanding of Earth's water and energy cycle (Hou et al. 2014). Specifically, the goal of GPM's Ku- and Ka-band radars is to provide measurements of microphysical properties and vertical structure information over a broad spectral range. Given that the reflectivity detection threshold for GPM is much higher than for *CloudSat*, GPM is better suited to retrieve the higher snow precipitation rates.

Evaluations of the retrievals of IWC and S from these active spaceborne sensors are clearly needed. Protat et al. (2010) presented a statistical analysis of the IWC of tropical ice clouds as derived from three years' worth of ground-based radar/lidar retrievals at the Darwin ARM site in Australia's Northern Territory and compared them with the same statistics derived from the microphysical retrieval methods 2B-CWC-RO and 2B-CWC-RVOD. They found that the mean vertical profile of IWC is overestimated below 10-km heights, with peak values off by a factor of 2. In a second evaluation, Norin et al. (2015) quantitatively intercompared snowfall estimates from a ground-based polarized C-band Doppler radar in Sweden to *CloudSat* estimates when the satellite passed overhead in the vicinity of the radar. Taking only those comparison cases where the radar and *CloudSat* measurements were relatively collocated (~30 km), they concluded that the 2C-SP retrieval algorithm (Wood et al. 2013) has limited ability to retrieve at the higher end of the snowfall intensity distribution ($>1\ \mathrm{mm\ h^{-1}}$). For lower snowfall rates, both the Swedish radars and *CloudSat* seem to suffer from limitations. While the ground-based radars are capable of detecting even nonprecipitating low-intensity echoes, range-dependent sensitivity limits and overshoot cause retrieval issues for more distant snowfall events. For *CloudSat*, 2C-SP retrievals are limited to reflectivities above about $-15\ \mathrm{dB}Z$, and the lowermost few radar bins, ranging up to 600–1200 m above ground level, are affected by ground clutter (the so-called radar blind zone), causing shallow events to go undetected. Thus, it was difficult for them to compare snowfall events. Assessments of GPM's capability to reliably measure rain and snow precipitation, both at the surface and aloft, are under way.

Data from in situ microphysical measurements provide an opportunity to evaluate, in a statistical sense, the accuracy of retrievals from satellite and climate models. The 2C-ICE retrieval algorithm uses a combination of *CloudSat* reflectivities and *CALIPSO* extinction to derive various microphysical quantities, including IWC. Deng et al. (2010) applied this algorithm to radar–lidar measurements from the NASA ER-2 aircraft for one case study during the Tropical Composition, Cloud and Climate Coupling (TC4) Experiment. They tested the algorithm during periods when the NASA DC-8 aircraft sampled in situ almost directly below the ER-2, making measurements of the ice water content with a counterflow virtual impactor (CVI) probe. The CVI probe is an inlet with a downstream total water instrument measuring the evaporated cloud particles. The median and mean values of the ratio of $\mathrm{IWC_{CVI}/IWC_{2C\text{-}ICE}}$ were 1.05 and 1.21 ± 2.51, respectively (Deng et al. 2013). For a TC4 case when the DC-8 underflew *CloudSat*/*CALIPSO*, the median and mean ratios of the $\mathrm{IWC_{CVI}/IWC_{2C\text{-}ICE}}$ were 1.31 and 1.74 ± 3.2, respectively. Deng et al. (2013) applied the 2C-ICE retrieval algorithm to *CloudSat*/*CALIPSO* data from the Small Particles in Cirrus (SPARTICUS) field program, when an in situ aircraft was making measurements concurrently. Although the IWC was not directly measured—it was estimated from the particle size distribution (PSD) data—the retrievals and in situ estimates agreed favorably. Khanal and Wang (2015), using measurements from a W-band radar–lidar combination from flights over Colorado, related the IWCs retrieved from the 2C-ICE algorithm to the IWCs measured on board the same aircraft for temperatures ranging from −10° to −40°C.

Statistical analysis showed that the mean difference between the retrieved IWC and the IWC derived from the PSD was about 26% for all ice clouds sampled. With the recent GPM field campaigns, including the Light Precipitation Verification Experiment (LPVEX) in 2010, the Midlatitude Continental Convective Clouds Experiment (MC3E) in 2011, the GPM Cold-Season Precipitation Experiment (GCPEX) in 2012, the Integrated Precipitation and Hydrology Experiment (IPHEx) in 2013, and the Olympic Mountain Experiment (OLYMPEX) in 2015, where in situ aircraft were either underflying radars on board overflying aircraft or overflying ground-based radars, opportunities now exist to evaluate retrieval algorithms over a wide range of cloud conditions (see Hou et al. 2014).

In situ aircraft observations provide another data source for evaluating model representations of ice microphysics. Eidhammer et al. (2014) compared aircraft in situ IWC measurements with model data that were derived by using the Community Atmospheric Model, version 5 (CAM5), global climate model. The observations were taken from two field campaigns with contrasting conditions: the Atmospheric Radiation Measurements Spring Cloud Intensive Operational Period in 2000 (ARM-IOP), which was characterized primarily by midlatitude frontal clouds and cirrus, and TC4, which was dominated by anvil cirrus. The model underestimated the higher moments of the PSD (second through fifth), with the third moment being approximately the ice water content. The mass-weighted terminal fall speed, which, when multiplied by the third moment, is approximately the snowfall rate, was lower in the model than in the observations; thus, the snowfall rate would have been underestimated as well.

Krämer et al. (2016) compiled a set of IWC measurements from 17 field programs over Europe, Africa, the Seychelles, Brazil, Australia, the United States, and Costa Rica, totaling 94 h of in situ data. The IWC measurements as a function of temperature were compared with model simulations. The Model for Aerosol and Ice Dynamics (MAID), a detailed microphysical box model, was run over the temperature range −83° to −43°C and with constant vertical velocities of 0.01, 0.1, 0.5, 1.0, and 3.0 m s^{-1}, and with fluctuating velocities as well. They found that there was good agreement between the IWC observations and the simulations.

Reliable, globally distributed in situ data are clearly needed for evaluating the accuracy of ice microphysics in climate models. Satellite measurements provide one such source, but the reliability of the retrievals has been evaluated only for limited areas that are mostly over continental regions. Rarely have there been intercomparisons of aircraft in situ measurements and climate model simulations. In this study, we use the in situ dataset reported by Krämer et al. (2016) and papers referenced therein in combination with a very large dataset reported by Heymsfield et al. (2013) to intercompare IWC and S derived from in situ data, satellite active remote sensors, and climate models as a function of temperature and geographic region. The goal of this intercomparison is to identify strengths and weaknesses in each of these methods, with the hope that this evaluation can lead to improved global modeling of ice cloud properties. The datasets used in this analysis are described in section 2, and the results are presented in section 3. Section 4 discusses the comparisons, and section 5 summarizes the results of the intercomparisons and draws conclusions.

2. Data

a. *In situ data*

1) SLK DATASET

The IWC dataset, hereinafter referred to as SLK, was compiled for this paper from the work of Schiller et al. (2008), Luebke et al. (2013), and Krämer et al. (2016). The geographical range is from 75°N to 25°S and the temperature ranges from −25° to −91°C. The field programs associated with the combined SLK dataset are identified in Table 1. Schiller et al. (2008) presented 10 h of IWC measurements from nine campaigns (1999–2005), using the Lyman-alpha fluorescence hygrometer (FISH) to measure the total water amount and another Lyman-alpha fluorescence hygrometer (FLASH) or an open-path tunable diode laser hygrometer [the Open-Path Jülich Stratospheric Tunable Diode Laser (TDL) Experiment (OJSTER)] to detect the water vapor content. Luebke et al. (2013) extended this dataset by 28.4 h of IWC measurements from four campaigns (2002–08), using the closed-path laser hygrometer (CLH) together with the open path TDL JPL Laser Hygrometer (JLH). Another 60.6 h of IWC observations from five campaigns (2011–14) were added to the dataset by Krämer et al. (2016). For two of the campaigns, FISH and CLH were used to measure the IWC. During three other field experiments, IWC was derived from particle size distributions over the size range 0.6–950 μm.

For the SLK dataset, the estimated uncertainty is ±7%–20%. The lower limit of the dataset is 10^{-6} g m^{-3} with some points down to 10^{-7} g m^{-3}. A reasonable upper limit is 0.3 g m^{-3}. The SLK dataset contains 93.6 h of 1-Hz IWC measurements, totaling about 156 000 1-Hz

TABLE 1. Summary of airborne field program datasets accessed during this study. The following regions are listed in the final column: P, polar; M, midlatitude; and T, tropics.

Acronym	Field program	Year	Region
SLK dataset			
ACRIDICON	Aerosol, Cloud, Precipitation, and Radiation Interactions and Dynamics of Convective Cloud Systems	2014	T
APE-THESEO	Airborne Platform for Earth Observation—(contribution to the) Third European Stratospheric Experiment on Ozone	1999	T
AIRTOSS	Aircraft Towed Sensor Shuttle	2013	M, P
CIRRUS 2003		2003	M
CIRRUS 2004		2004	M, P
CIRRUS 2006		2006	M
COALESC	Combined Observation of the Atmospheric Boundary Layer to Study the Evolution of Stratocumulus	2011	M
CRYSTAL-FACE	Cirrus Regional Study of Tropical Anvils and Cirrus Layers–Florida-Area Cirrus Experiment	2002	T
ENVISAT	European Space Agency's *Environmental Satellite*	2002	M
ENVISAT		2003	M, P
EUPLEX	European Polar Stratospheric Cloud and Lee Wave Experiment	2003	P
MACPEX	Midlatitude Airborne Cirrus Properties Experiment	2011	M
MidCiX	Middle Latitude Cirrus Experiment	2004	M
ML-CIRRUS	Midlatitude Cirrus	2014	M
SCOUT-03	Stratospheric-Climate Links with Emphasis on the Upper Troposphere and Lower Stratosphere (UTLS)	2005	T
START08	Stratosphere–Troposphere Analyses of Regional Transport	2008	M, P
TC4	Tropical Composition, Cloud and Climate Coupling Mission (NASA WB57 mission)	2006	T
TROCCINOX	Tropical Convection, Cirrus, and Nitrogen Oxides Experiment	2005	T
H16 dataset			
AIRS-II	Alliance Icing Research Study II	2003	M
ARM	Atmospheric Radiation Measurement	2000	M
C3VP	*CloudSat*/*CALIPSO* Validation Project	2007	M
CRYSTAL-FACE		2002	T
FIRE-II (Rep)	First International Satellite Cloud Climatology Project (ISCCP) Regional Experiment	1991	M
ICE-T	Ice in Clouds Experiment-Tropical	2011	T
MPACE (MP)	Mixed-Phase Arctic Cloud Experiment	2004	P
NAMMA	NASA's African Monsoon Multidisciplinary Analyses	2006	T
PreAVE (SV)	Pre-Aura Validation Experiment	2004	T
SCOUT (SCT)	Stratospheric-Climate Links with Emphasis on the UTLS	2005	T
TC4	Tropical Composition, Cloud and Climate Coupling Mission (WB57)	2006	T

data points, corresponding to about 67 000 km of in-cloud sampling.

2) H16 DATASET

In another comprehensive study, Heymsfield et al. (2013) reported on PSDs and direct measurements of IWC from 10 aircraft field programs, spanning latitudes from the Arctic to the tropics and temperatures from −86° to 0°C. This dataset is augmented here with data from the Ice in Clouds Tropical Field Program, based out of St. Croix, Virgin Islands (Heymsfield and Willis 2014). The combined dataset is referred to as H16 [H13 + Ice in Clouds Experiment-Tropical (ICE-T)]. It includes the field programs identified in Table 1, containing about 260 000 data points, averaged over 5-s intervals, with an in-cloud pathlength of about 260 000 km. For temperatures of −60°C and above, IWC was measured by the CVI probe, with a measurement range of 0.01–2.0 g m^{-3}. Below −60°C, 7% of the IWC observations used the CVI and 93% used the FISH instrument, with the lower detection level stated for the SLK dataset. The latter data were all from the Stratospheric–Climate Links with Emphasis on the Upper Troposphere and Lower Stratosphere (SCOUT-03). There is overlap here with the SLK dataset. Because there have been few data collected at such low temperatures, these SCOUT data from both datasets are included here.

The measured ice water contents in the H16 dataset were used to develop temperature-dependent mass-dimensional relationships of the form $m = aD^b$ over

the temperature range 0° to −86°C. For every 5-s period, the coefficient b was derived using fractal geometry based on the measured particle cross-sectional areas (giving a value of b of about 2.1), and the coefficient a was derived from the PSD (50 μm to >1 cm) that gave the measured IWC (when hysteresis of the CVI output, mostly due to periods with exiting clouds, was filtered out). The development of temperature-dependent a and b coefficients facilitated the use of the PSDs to estimate the IWC for periods when the IWC was below or above the measurement range of the CVI. This was necessary for 25% of the time. For the times when the IWC exceeded the CVI threshold, the median ratio of the IWC derived from the PSD to those derived from the CVI was 1.00, but the average ratio was 1.19 ± 3.1. Based on this evaluation and given the inherent uncertainty of the particle size distributions at low number concentrations and the masses of small particles, we have chosen to use a lower cutoff of 10^{-4} g m^{-3} for our analysis.[1] The potential impact of this detection threshold is discussed further in section 3. With a lower cutoff of 0.0001 g m^{-3}, the dataset comprises a total of 90 000 (5-s average) points. Increasing the cutoff from 0.000 01 to 0.0001 g m^{-3} raises the median IWC from 0.037 85 to 0.038 42, or by only 1.5%. The total combined in-cloud horizontal sampling distance in the H16 study is about 89 000 km.

In total, the combination of the Schiller et al. (2008), Luebke et al. (2013), Krämer et al. (2016), and Heymsfield et al. (2013) datasets contains about 343 000 km of in-cloud sampling.

b. *Models*

1) CAM5 MODEL AND OUTPUT

This study uses version 5 of the Community Atmosphere Model (Neale et al. 2010) with a two-moment scheme (Morrison and Gettelman 2008), which also includes ice supersaturation (Gettelman et al. 2010) and an advanced cloud macrophysics (fraction) scheme (Park et al. 2014). CAM5 also includes a prognostic aerosol model (Liu et al. 2012) and a moist boundary layer scheme (Bretherton and Park 2009). CAM5 is available as part of Community Earth System Model release 1.0 (CESM1; Hurrell et al. 2013). To this version of CAM5, a new version of the cloud microphysics scheme has been added (Gettelman and Morrison 2015) with a prognostic representation of precipitation (snow and rain).

The model was run for 3 yr with climatological year 2000 sea surface temperatures (SSTs) and greenhouse gases. Resolution is 1.9° × 2.5° in the horizontal, with 30 levels in the vertical to 3 hPa.

2) MET OFFICE UNIFIED MODEL

The Met Office Unified Model is used routinely for operational weather and climate prediction. The model uses parameterizations to represent the cloud fraction (Wilson et al. 2008); large-scale stratiform mixed-phase cloud microphysics (Wilson and Ballard 1999); deep, midlevel, and shallow convection (Gregory and Rowntree 1990); and boundary layer mixing (Lock et al. 2000). The convection representation has a simple microphysical representation and diagnoses the phase of the condensate associated with convection using a linear ramp ranging from all liquid at −10°C and warmer to all ice at −20°C and colder. The large-scale precipitation is capable of representing supercooled liquid water. It was run in a climate for 1 yr (1989) mode with a grid spacing of 1.9° × 1.25°. The model configuration used was Global Atmosphere 7 (GA7). Differences in the treatment of cloud from GA6 include the introduction of an updated ice cloud and radiation treatment, such as a new ice PSD treatment and associated modifications to the large-scale cloud fraction scheme (e.g., Furtado et al. 2015) and changes to the CAPE clouds for deep and midlevel convection. The monthly mean in cloud IWC (grid-box-average IWC/cloud fraction) diagnostic and temperatures were output from the microphysics for the stratiform precipitation. A threshold minimum in-cloud IWC and cloud fraction of 1×10^{-6} kg kg^{-1} and 0.0001, respectively, were required to record a nonzero in-cloud IWC value. For the convection a diagnosed IWC (consistent with the values used for the radiation) was combined with the stratiform cloud fraction in the same grid box.

c. *CloudSat*/CALIPSO *and GPM satellite retrieval products*

The *CloudSat* CPR makes near-nadir-pointing observations with a footprint of about 1.7 km along track by 1.3 km cross track between 82°N and 82°S. Data used for these analyses cover 2007–10. Meteorological state information comes from reanalysis products developed by the European Centre for Medium-Range Weather Forecasts (ECMWF) that have been

[1] As a sensitivity study, the minimum IWC derived from the PSDs for temperatures above −60°C was adjusted from 10^{-7} to 10^{-2} g m^{-3} in increments of an order of magnitude. The resulting ratio of the number of points included in the analysis to the total number of points for IWC of 10^{-7} g m^{-3} is as follows: 10^{-7}, 10^{-6}, 10^{-5}, 10^{-4}, 10^{-3}, and 10^{-2} g m^{-3} are 1.00, 1.00, 0.998, 0.991, 0.96, and 0.74, respectively.

collocated to the *CloudSat* radar profiles. The 2C-SP data are from the release 4 (R04) product series, while the 2C-ICE data are produced by an improve version of that algorithm (Deng et al. 2015).

1) 2C-ICE PRODUCT

The *CloudSat* Ice Cloud Property Product contains retrieved estimates of the IWC for identified ice clouds measured by the *CloudSat* CPR and the *CALIPSO* cloud–aerosol lidar. This 2C-ICE cloud product uses combined inputs of the measured radar reflectivity factor from *CloudSat* and the measured attenuated backscattering coefficients at 532 nm from the *CALIPSO* lidar to constrain the ice cloud retrieval more tightly than the radar-only product and to generate more accurate results. When the reflectivities are below the CPR's detection limit, *CALIPSO*-only data are used to retrieve the IWC; CPR-only data are used when *CALIPSO* data are not available.

2) 2C-SNOW-PROFILE PRODUCT

The 2C-SP retrieval algorithm estimates vertical profiles of the probability density functions (PDFs) of snow PSD parameters using explicit a priori assumptions about the snow particle microphysical and scattering properties. The estimates of the PSD parameters are then used along with the microphysical properties to construct the vertically resolved snowfall rate and, as in the study here, the ice water content. A retrieval is performed if the 2C-PRECIP-COLUMN product (Haynes et al. 2009) has categorized the surface precipitation as snow or as mixed phase with a melted mass fraction of less than 10%.

3) GPM

The satellite measurements cover approximately 65°S–65°N in a non-sun-synchronous orbit. The GPM dual-polarization radar consists of Ku-band (13.6 GHz) and Ka-band (35.5 GHz) channels. The data product used here is derived from level 2A processing, containing radar reflectivities and the retrieved precipitation rate and phase (Iguchi et al. 2010). Precipitation rate is retrieved from the radar reflectivity factor corrected by a hybrid of the Hitschfeld–Bordan (Hitschfeld and Bordan 1954) method and a surface reference method. The snowfall retrievals used in the study are based on the combined Ku- and Ka-band observations. The reflectivities shown in the figures below are from the Ku band. The horizontal resolution is about 5 km. The data are from the period 8 March 2014–31 March 2015.

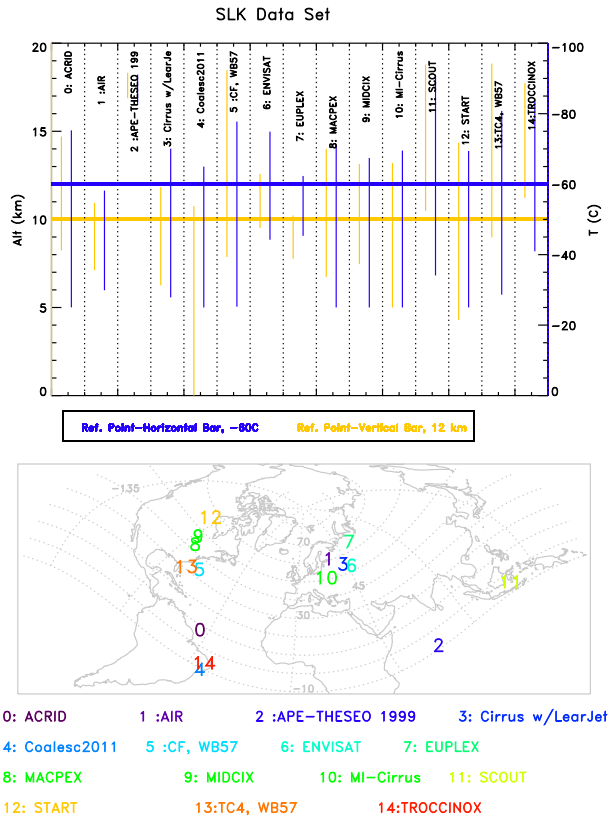

FIG. 1. Summary of data collected in the SLK dataset. (top) Altitude and temperature ranges for each of the field programs. (bottom) Geographical distribution of the dataset.

3. Results

This section presents data derived using the methods identified in section 2, intercomparing the datasets according to geographical region.

a. *Summary of in situ measurements*

Figures 1 and 2 show the temperature, altitude, and geographical distributions of the SLK and H16 datasets, respectively. For reference, polar regions are defined here as above +60° latitude and below −60° latitude, midlatitude regions from −30° to −60° and +30° to +60° latitude, and the tropics as −30° to +30° latitude; these areas comprise 13%, 37%, and 50% of the earth's surface area, respectively.

For SLK, the data (Fig. 1) for polar regions are all from the Arctic (P; right column, top of Table 1) and from the midlatitudes (M; Table 1) and tropics (T; Table 1). For H16, the polar data include data from the Arctic (P; right column, bottom of Table 1), the midlatitudes (M), and the tropics (T). Of the latter, NAMMA and ICE-T are associated either directly or indirectly with deep convection.

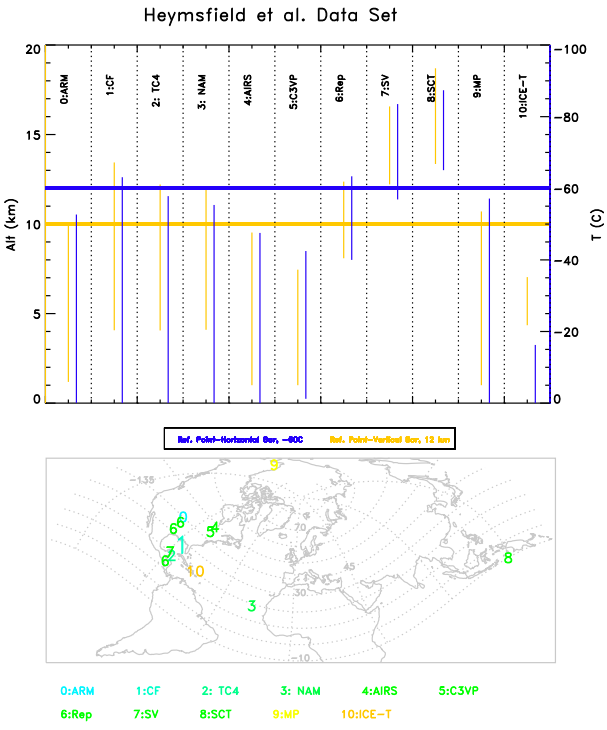

FIG. 2. As in Fig. 1, but for the H16 dataset.

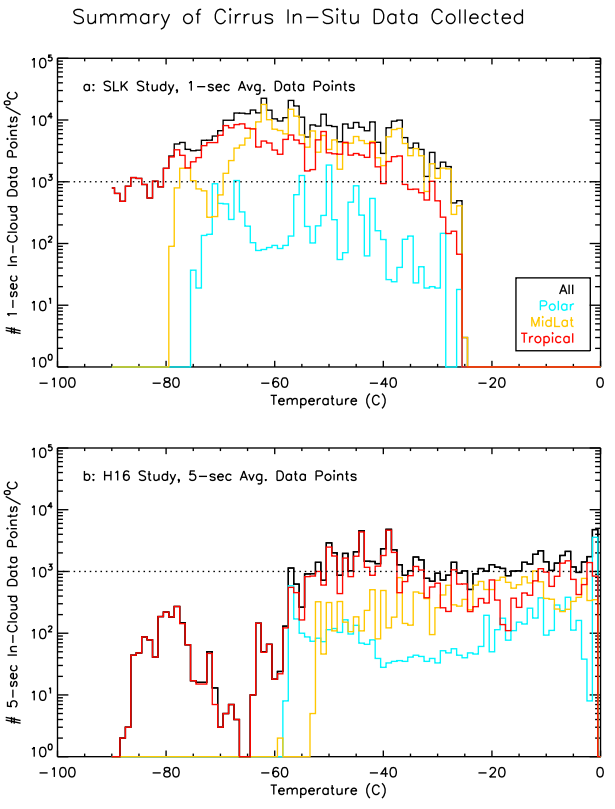

FIG. 3. Summary of the number of periods in cloud for the two in situ datasets: (a) SLK and (b) H16. Note that different averaging periods were used in the two datasets.

Figure 3 shows the temperature distribution of the measurements for the two in situ datasets. As noted for SLK (Fig. 3a), the temperatures sampled were all below about −25°C and extended to a temperature as low as −91°C. Across this temperature range, a large sample of data was collected, especially at temperatures from −70° to −40°C. The tropical data extended to the lowest temperatures. For the polar clouds, relatively few in situ measurements were collected. The midlatitude data were primarily at temperatures between −60° and −40°C and included most of the SLK data in that temperature range.

The temperature distribution for the 5-s average data from H16 shows fewer points, so to make it comparable to the 1-s data reported in SLK, the number of points should be multiplied by a factor of 5. Temperatures sampled during H16 were from about −88° to >0°C. The temperatures for the tropical dataset also extend to low temperatures. A reasonably large set of data was collected in the tropics for temperatures warmer than −50°C in part because of three field programs: TC4, NASA's African Monsoon Multidisciplinary Analyses (NAMMA), and ICE-T. Many of the in situ data points collected during NAMMA and ICE-T were in recorded in convective regions, but we have removed those times when there was liquid water present in concentrations >0.01 g m^{-3} because we want to focus on the distribution of the IWC with temperature. As with the SLK, most of the data at temperatures warmer than −50°C are from midlatitude clouds.

b. *Ice water content comparisons*

1) IWC AND ICE WATER MIXING RATIO COMPARISONS FOR THE INDIVIDUAL DATASETS

This section examines the temperature dependence of the ice water content for the various datasets. Comparing the IWCs solely as a function of temperature can potentially introduce errors because a given temperature can correspond to widely different atmospheric pressures. For example, a temperature of −40°C can correspond to pressures of 900 hPa in the Arctic and 300 hPa in the tropics. For this reason, we have also examined the temperature dependence of the ice water content mixing ratio (IMX, which is the IWC divided by the air density).

In what follows, a curve identified as the $\Delta\rho$ curve or reference curve is used as a benchmark to intercompare the various datasets (Fig. 4). To first order, the IWC is approximately given by the difference in the density of the water vapor between the RH required for ice

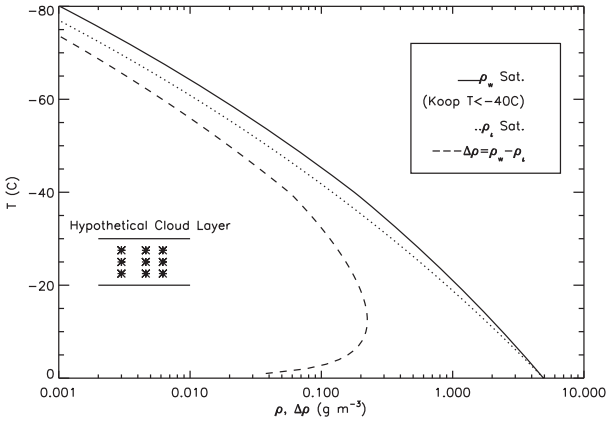

FIG. 4. Saturation vapor densities with respect to water and ice as a function of the air temperature. The difference between the two saturation vapor densities, $\Delta\rho$, yields the reference IWC curve as a function of temperature. A schematic of the process is illustrated in the hypothetical cloud layer.

nucleation (solid curve labeled ρ_w in Fig. 4) and the RH at ice saturation (ρ_i, dotted curve in Fig. 4). At temperatures −40°C and above, ρ_w is the density of the water vapor at saturation with respect to the liquid water at the given temperature and at temperatures below −40°C this vapor density is derived from the RH where homogeneous ice nucleation becomes significant (see Koop et al. 2000). The reference curve is given by this difference between ρ_w and ρ_i (Fig. 4, dashed curve). The idea is based on the following simplified view of the subsequent growth of the ice phase and the IWC (see schematic in the Fig. 4 inset). For temperatures of −20°C and below, where much of our analysis is focused, linear ice crystal growth rates are $<1\,\mu\mathrm{m\,s^{-1}}$ (Bailey and Hallett 2012). The ice crystals will largely grow in place with little fallout for a period of time, which will decrease the RH appreciably below the RH at the time of nucleation, approaching ice saturation. The crystals do fall out of the parcel, but those falling from above replace those falling out from that level, resulting in a slightly lower IWC, but given the rate of change of $\Delta\rho$ with temperature, this lower IWC would have an insignificant effect on the net change in the IWC (fall-in versus fallout). For outflow cirrus, the $\Delta\rho$ estimate would not be valid, because the ice mass might form at warmer temperatures and then flow out of high levels. Likewise, the $\Delta\rho$ estimate would not be valid in sublimation zones, either in stratiform or convective outflow situations or from cloud base to the surface, nor when liquid water is present. Note that in general, clouds that are in their ''active'' state (not dissipating) were sampled. At times, though, when constant altitude penetrations are made near cloud base, these are generally sublimation zones. As a first-order approximation, 10% of the measurements are in sublimation zones. Note that the $\Delta\rho$ curve is used only as a reference point for comparison with the various datasets. In addition, we have derived a reference mixing ratio curve by taking the reference IWC curve and dividing it by the air density using the *U.S. Standard Atmosphere, 1976*.

Figure 5 summarizes the distribution of the median IWC as a function of temperature for the various datasets; within each set the data are separated according to the climate zone. The three columns present the data from the in situ observations (Figs. 5a,b), model output (Figs. 5c,d), and *CloudSat* retrievals (Figs. 5e,f). To avoid clutter, standard deviations are not plotted in Fig. 5. For comparison, the reference $\Delta\rho$ curve is plotted. In general, the IWC increases with temperature, as is expected based on the reference curve plotted in each panel.

For the in situ observations the following points are noted. At temperatures −60°C and below, the SLK dataset is more geographically distributed than the H16 dataset. The IWCs at these temperatures are considerably below the $\Delta\rho$ curve for the SLK dataset and to a lesser extent for the H16 dataset. At temperatures from −25° to −60°C, the H16 data show a geographical dependence, with the IWCs highest in the tropics and lowest in the polar regions. This dependence is not found in the SLK dataset. The IWCs for the tropical and midlatitude clouds in H16 closely match the $\Delta\rho$ curve, and the IWCs from SLK are considerably below that curve. The reasons for the differences are discussed later in this section. At temperatures warmer than −25°C, the H16 IWCs closely match the $\Delta\rho$ curve, except for the polar clouds.

For both the CAM5 and U.K. models, the distribution of the mean IWC with temperature is generally parallel to the $\Delta\rho$ curve. The marked decrease in the CAM5 IWCs at temperatures warmer than −25°C for tropical regions is suggestive of an anomaly in the convective parameterization scheme, although at least some of it is due to the conversion of some of the condensate to liquid water rather than snow. It is also important to point out that the variables available for CAM5 include diagnostic ice water from the stratiform and deep convection schemes but not from the shallow convective scheme. As a result, in the tropics at warmer temperatures where shallow convection is active, some of the IWC is missing. For the U.K. data, the IWCs are close to the reference curve, and there is a strong dependence of the IWC noted on geographical location, with the largest values noted in tropical regions and lowest in polar regions.

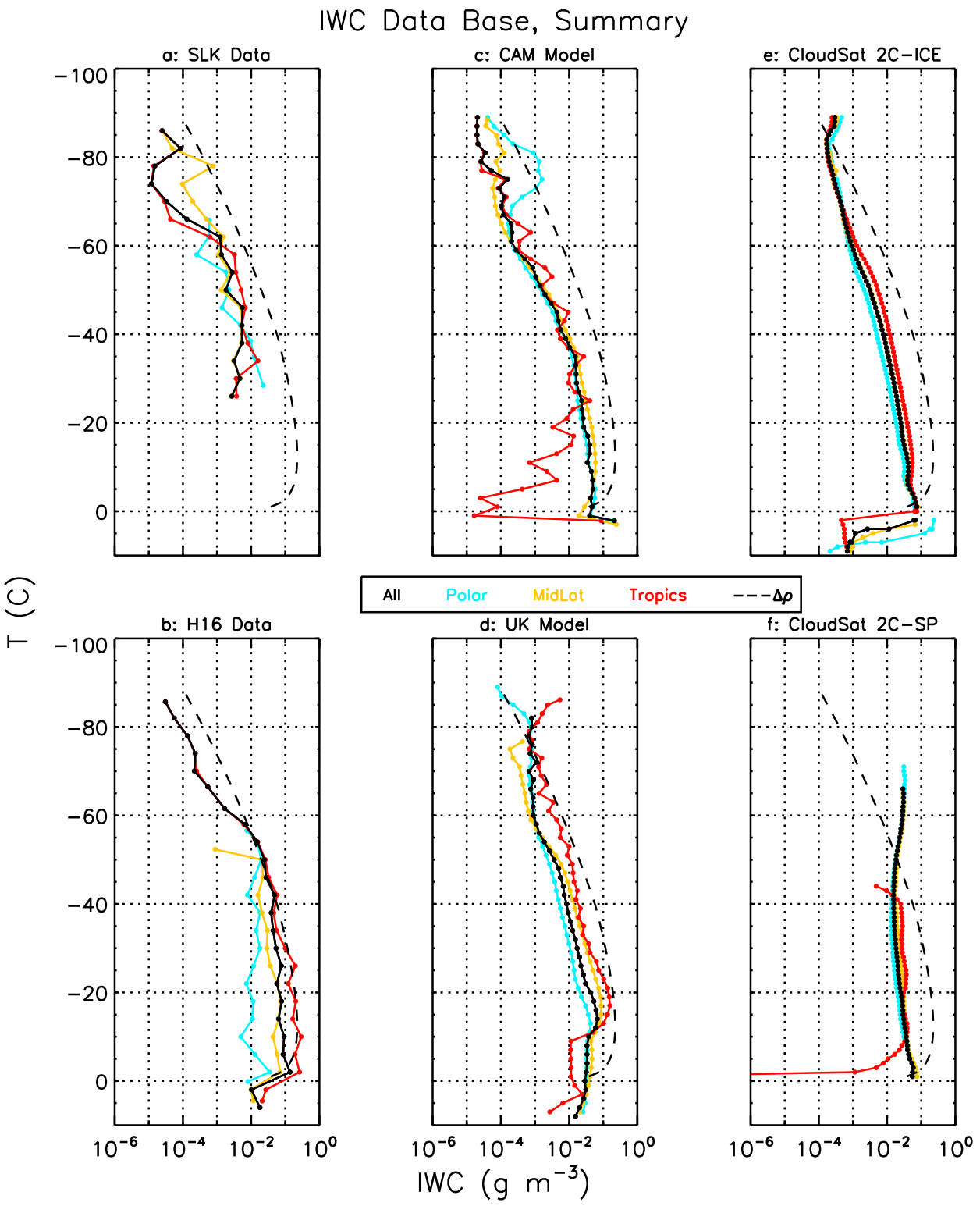

FIG. 5. Temperature distribution of the ice water content: (a) SLK dataset, (b) H16 dataset, (c) CAM5 model results, (d) Met Office model, (e) *CloudSat* 2C-ICE retrieval, and (f) *CloudSat* 2C-SP retrieval. In each panel, the data are separated according to latitudinal ranges: polar, midlatitudes, and tropics, along with the results for all regions combined. The legend is labeled across the center of the figure. The term $\Delta\rho$ is explained in the text.

The *CloudSat* 2C-ICE retrievals seem to be realistic in that for a given temperature, and transitioning from the tropical to polar regions, the IWCs shift to lower values. The *CloudSat* 2C-SP retrievals show almost no dependence on the geographical region and have patterns of behavior that do not follow the $\Delta\rho$ curve. The reason for this behavior is discussed later. Note that the 2C-SP formulation is such that IWC aloft is retrieved only when there is precipitation reaching the surface.

To address the question of whether the IWC–T relationship between different cloud types is significantly affecting the interpretations drawn from Fig. 5, we used the precipitating cloud-type flags from the *CloudSat* and GPM datasets to examine the percentage of precipitating clouds that are convective versus stratiform and the corresponding IWCs. With the greater sensitivity of the *CloudSat* radar, those data are used to derive the percentages. The observational and model datasets are not used in this evaluation because the observations are from a small subset of data and the models cover a large region where convection would have a relatively small effect. For a temperature of −20°C, polar, midlatitude, and tropical regions have the following frequency of occurrence for convective (stratiform) clouds: 16% (84%), 12% (88%), and 12% (88%), respectively. For a temperature of 0°C, these values become 13% (87%), 11% (89%), and 11% (89%), respectively. When both precipitating and nonprecipitating clouds are considered, the percentage of convective clouds is even smaller relative to the stratiform clouds. Thus, the IWC–T relationship is heavily weighted toward stratiform precipitating and nonprecipitating clouds in all regions. To examine whether there are significant differences in the IWC of precipitating convective and stratiform clouds, we derived median values of the IWCs for the stratiform and convective regions as a function of temperature. For a temperature of −20°C in the polar, midlatitude, and tropical regions, respectively, the convective (stratiform) clouds are 0.061 (0.039), 0.179 (0.090), and 0.22 (0.11) g m^{-3}. For a temperature of 0°C, these values become 0.18 (0.21), 0.29 (0.31), and 0.29 (0.30) g m^{-3}, respectively.

To summarize, a comparison of the various methods for deriving the temperature distribution of the IWCs shows differences between the data by collection method, geographical location, and temperature, and these are not likely to be due to the dominance of convective or stratiform clouds in each region. The data from H16 are generally fairly close to the $\Delta\rho$ curve with *CloudSat* somewhat lower, with the exceptions of the relatively lower values for the polar data and, in the case of H16, at temperatures −55°C and below. The SLK data for all geographical locations are lower than the $\Delta\rho$ curve, and all locations show about the same values. The CAM5 dataset follows the $\Delta\rho$ curve, but it is lower by about an order of magnitude, with the exception of the tropical dataset, which shows a steep drop-off at temperatures above −25°C. The values are fairly close to those of the SLK dataset. The U.K. values are also considerably lower than the $\Delta\rho$ curve, with the largest values noted in the tropical regions and the lowest in the polar regions, as would be expected.

Given the similarity between the trends observed for the IWCs and those found for IMX, we will not show a plotted figure but briefly note the differences. The *CloudSat* 2C-SP retrievals show a progression with temperature in IMX, from lower values in polar regions to higher values in the tropics, a much larger difference than was noted in IWC from this algorithm. The H16 data also show similarly larger differences. Because the differences noted between the IWC as a function of temperature and the ice mass mixing ratio as a function of temperature are not marked, the remaining discussion in this section will focus on the comparisons between the IWCs derived from the various methods.

We show the temperature dependence of the IWC as derived from all of the datasets, for all geographical regions combined (Fig. 6a) and for each region separately (Figs. 6b–d). When data from all the regions are combined (Fig. 6a), the H16 curve (red line) nearly overlays the $\Delta\rho$ curve (black dashed line), followed by the U.K. data (light green) and the 2C-ICE data (dashed, purple), with the SLK (orange) and CAM5 (cyan) data having about the same values, and the 2C-SP retrieval (dashed, green) displaying a parabolic profile.

In general, the highest IWCs are noted for H16 and the lowest for SLK for $T < -65$°C and $T > -40$°C. In the polar regions (Fig. 6b), both in situ datasets, although they track fairly closely in overlapping temperature ranges, display nonuniform changes in the IWC with temperature, which points to the relatively small sample of in situ observations there. The CAM5 and the U.K. model data are quite close to each other, except for temperatures below −60°C, where the latter dataset shows unexpectedly large values, and for temperatures above −25°C in tropical regions, where CAM values drop sharply (Fig. 6d). The IWCs retrieved from *CloudSat* 2C-ICE are generally close to those from CAM5 and the U.K. model, although there is an unexpected increase in the IWC at temperatures below about −75°C. The 2C-SP-retrieved IWCs show an unexpected increase in the IWCs at temperatures below about −30°C.

2) THE SLK AND H16 IN SITU DATASETS COMBINED

Because the individual datasets making up the SLK and H16 have been published in the formal literature and have been and will be used in future studies, it was

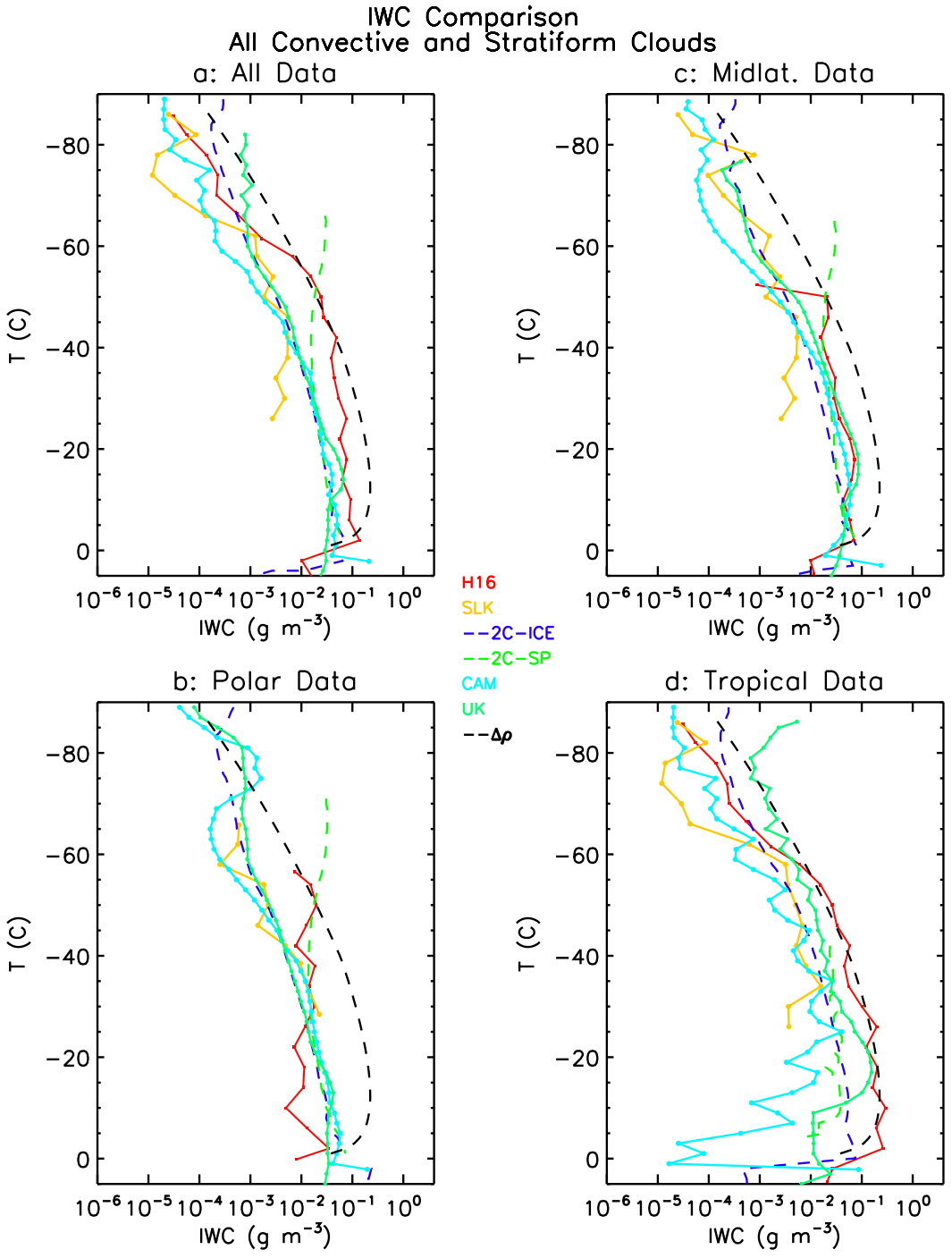

FIG. 6. Ice water content as a function of temperature, grouped for (a) all regions and cloud formation mechanisms combined, (b) polar regions, (c) midlatitude regions, and (d) tropical regions. The legend appears in the center of the figure. The solid lines depict the in situ data and model output, and the colored dashed lines depict the *CloudSat* retrievals.

appropriate to represent them separately, as in Figs. 5 and 6. We now seek to find the reasons for the differences between the SLK and H16 datasets. The distribution of IWC with temperature is shown in increments of an order of magnitude from 10^{-7} to 10^{-2} g m^{-3} for the SLK and H16 datasets in Fig. 7. For each temperature interval, Fig. 7 shows the fraction of data points in a given IWC interval to the total number of points with IWCs above 10^{-7} g m^{-3}. What is clearly noted is that, aside from the lowest temperature range sampled, the

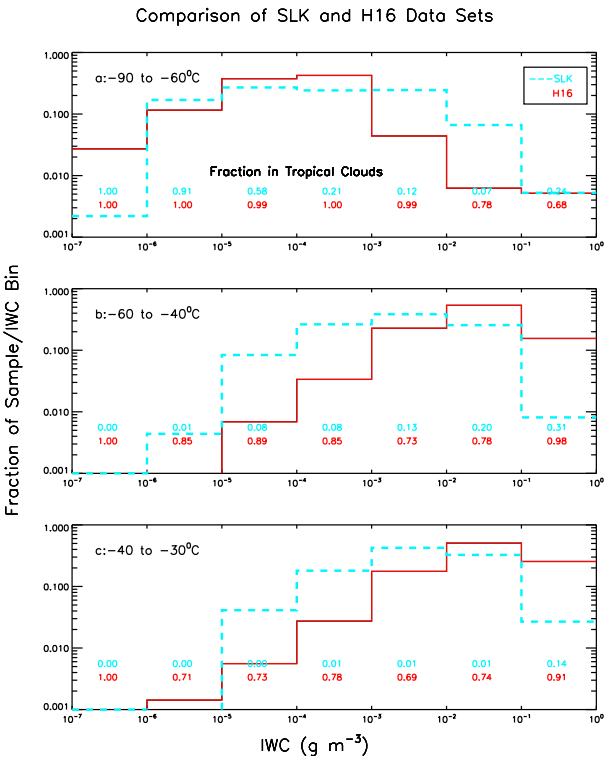

FIG. 7. (a)–(c) In three intervals of temperature, the fraction of the total number of data points for IWCs of 10^{-7} g m^{-3} and above that fall within a given IWC bin, separately for the SLK and H16 datasets. The numbers in each panel are the fractions of data points in that IWC interval that are from cirrus at tropical locations.

H16 IWCs are considerably larger than those in the SLK dataset. Also shown in each panel is the fraction of the total number of data points in a given IWC interval that is derived under tropical conditions, which is usually associated with the outflow from convection. From Fig. 7, it can be concluded that the reason for the larger IWCs in H16 than SLK is due to the sampling in the former case being heavily weighted toward tropical clouds and in the latter case toward midlatitude, nonconvectively generated ice cloud. For this reason, it seems prudent to combine the two datasets to get a more comprehensive view of the global distribution of cirrus cloud IWCs. Not combining the two datasets may lead to errors in interpretation and comparisons with satellite and model data, because SLK sampled lower IWCs and H16 higher IWCs. Although the H16 dataset was derived for 5-s averages, each 5-s average (T, IWC) data point is considered five times to make the two datasets consistent.

Figure 8 compares the median values of IWC as a function of temperature for the SLK dataset, the H16 dataset, and the combined dataset. A comparison of the curves in Fig. 8 shows some interesting results. On average, for $T < -80$°C, the SLK IWCs dominate; for $-60° < T < -55$°C, both datasets have about the same IWCs; and for $T > -55$°C, the H16 values dominate. These differences might be attributable to the different IWC sampling ranges for the two studies. For example, for $T > -55$°C, the IWCs, especially in the tropical convective ice clouds, can contribute IWCs much larger than 0.3 g m^{-3}.

A depiction of the mean and variance of the IWCs with temperature for the combined SLK and H16 dataset is presented in the form of cumulative PDFs in Fig. 9, with PDFs shown in 10% increments beginning with the interval 0.25–0.35 and ending with 0.75–0.85. The combined dataset shows a relatively smooth profile of IWC and small variance with temperature when the data from all geographical locations are combined (Fig. 9a). This smoothness and narrowness of the IWC distribution is also found for the midlatitude and tropical regions (Figs. 9c,d). What is interesting about the polar data is the small decrease in the IWC with temperature when compared with the other regions (Fig. 9b). Exponential fits to the IWC data in each panel fit the data quite well, with the exception of the tropical regions at temperatures above −10° and below −70°C.

3) COMPARISONS OF IWC DERIVED FROM MODEL AND SATELLITE DATA

Figure 10 is in a form similar to Fig. 9, with the CAM5 data in the left panels and the U.K. data in the right panels, enabling a comparison of the in situ and model data. For each 2°C, median values of IWC and S when ice cloud is present are derived from the model and satellite datasets. For temperatures below −30°C, the IWC profiles for the combined, midlatitude, and tropical datasets are quite similar to those found for the in situ data, whereas the IWCs for the polar regions are generally considerably larger. As temperatures warm above −20°C, the IWCs for the CAM5 data for tropical regions decrease, as noted earlier. What is noticeable in comparing the CAM5 with in situ data is that the spread of IWCs at a given temperatures (width of the colored regions, 20%–80% of the data points) is much larger in the latter than former. The IWCs in the U.K. model results are quite close to the median values found from the in situ data, but the spread of the IWCs is much narrower than that of the in situ data. The difference in spread is to be expected, given that the models represent a single value for ice water content over 25–200-km grid boxes. For a proper comparison of variance, the in situ observed IWC should be averaged on the scale of model IWC × cloud fraction.

The cumulative probability distribution for the *CloudSat* 2C-ICE retrievals is close to those for the

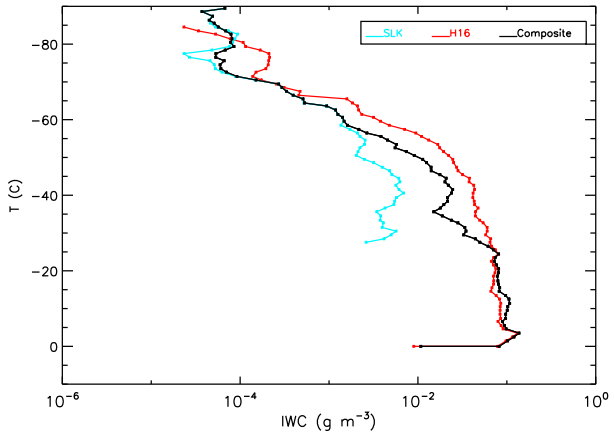

FIG. 8. IWCs, averaged in temperature increments of 1°C, as a function of temperature for the SLK and H16 datasets separately and combined. Each of the data points is smoothed over 5°C using a smoothing routine, to increase the clarity. Each H16 (IWC, T) data point is considered five times to account for the different sampling intervals in each study. For $T > -26$°C, the H16 and combined datasets have the same values.

in situ data for the combined dataset and geographically, although the spread of the IWCs is considerably larger for the 2C-ICE data (Figs. 11a–d). By contrast, there are marked differences between the 2C-SP retrievals and the in situ data, although the spread of the IWCs is much smaller (Figs. 11e–h).

c. *Snowfall rate comparison*

Using the PSD and the ice particle terminal velocity estimates from the Heymsfield et al. (2013) study, snowfall rates were derived for the H16 dataset by integrating the product of the mass times the terminal velocity across the measured PSDs. Because the snowfall rates were not derived directly from either the SLK in situ data or for the *CloudSat* 2C-ICE retrievals, the relationships between snowfall rate, ice water content, and atmospheric pressure (for P = 1000, 800, 600, and 400 hPa) from Heymsfield et al. (2013) are used to derive the snowfall rate from the ice water content and associated pressure for those studies. We have also developed a method to create a "reference" snowfall rate–temperature dependence. For each PSD from the H16 dataset, a mean mass-weighted terminal velocity V_m can be found from

$$V_m \ (\mathrm{cm\,s^{-1}}) = S \ (\mathrm{mm\,h^{-1}})/0.036\mathrm{IWC} \ (\mathrm{g\,m^{-3}}). \quad (1)$$

A relationship between V_m and IWC for pressure levels of P = 1000, 800, 600, and 400 hPa can be derived, and a pressure-dependent V_m–IWC relationship can be developed (Fig. 12). Using this summary relationship, a reference value for S_{th} as a function of temperature and height is derived from the reference ($\Delta\rho$) IWC from

$$S_{th} \ (\mathrm{mm\,h^{-1}}) = 0.036 V_m \mathrm{IWC}_{th}, \quad (2)$$

where IWC_{th} is the reference IWC value at a given temperature and the pressure level for the calculation of V_m is assumed to be the pressure from the standard atmosphere for that temperature.

The snowfall rates derived for each dataset and subdivided according to regions follow along the same relative trends as noted for the IWC comparison (cf. Figs. 13 and 5). Because the SLK data do not extend to temperatures above −26°C and the H16 data are mostly from temperatures above about −60°C (Figs. 13a,b), comparisons between the two datasets can be made for $-60° < T < -26$°C. The SLK data do not show a regional temperature dependence, whereas the H16 data show decreasing snowfall rates from tropical to polar regions. The snowfall rates for the model data are about an order of magnitude lower than the H16 rates, with little regional dependence (Figs. 13c,d). The CAM5 snowfall rates for the tropical regions decrease as temperatures warm above about −25°C, mirroring the trends noted for IWC. The 2C-ICE-retrieved snowfall rates, derived from the H16 S–IWC relationship, are similar in magnitude to those for the H16 dataset. In contrast, the 2C-SP-retrieved snowfall rates have little similarity to either the 2C-ICE or H16 rates (Figs. 13b and 13e). The snowfall rates derived from the GPM Ku-band radar data are higher than those from the in situ or *CloudSat* data, because of the higher reflectivity detection threshold of the GPM Ku-band radar. Surprisingly, the S profile for the GPM retrievals is similar to that noted for the 2C-SP retrievals, although the average values of S are higher for the GPM dataset. Note that both the 2C-SP- and GPM-retrieved snowfall rates increase at temperatures below about −30°C. The trends for an increase in the snowfall rate with decreasing temperature can be linked to the fixed precipitation detection reflectivity thresholds used in the retrievals.

The combined SLK and H16 snowfall rates (Fig. 14), plotted in a PDF-type form to show the variability, exhibit a nearly monotonic (exponential) decrease with temperature (see dotted curves, which are exponentials). The highest rates are noted in the tropical regions (Fig. 14d), and the lowest values are found in the polar regions (Fig. 14b).

Cumulative probability distributions of S as a function of temperature from the model datasets in the form of PDFs are compared with each other and with the average from the in situ observations (dashed lines)

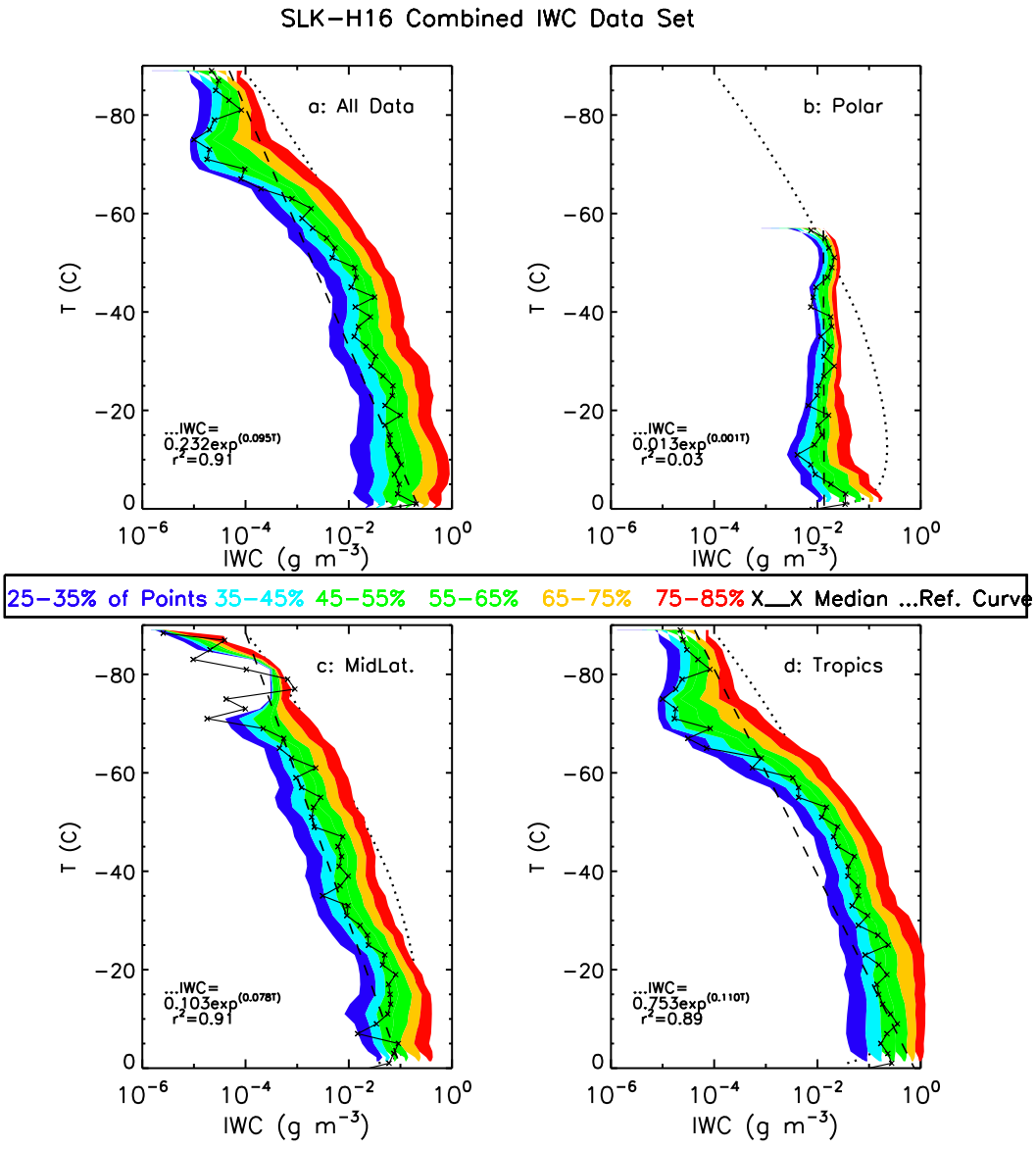

FIG. 9. Cumulative probability distributions of the IWC as a function of temperature from the combined SLK and H16 dataset. The ranges used to accumulate the number of points are color coded, and the dark dashed line shows the median values. The dotted line is a curve fit to the IWC-T median values, with the fit indicated.

in Fig. 15. At a given temperature, there is a wide distribution of S for the CAM5 data (Fig. 15, left panels) and a narrower distribution for the UK data (Fig. 15, right panels). The U.K. model data extend to lower temperatures than those for CAM5. The two datasets yield comparable snowfall rates with temperatures (Figs. 15a,e). The rates derived for polar regions for the two models at overlapping temperatures are comparable, and the trends and magnitudes are similar to the median values derived from in situ data (Figs. 15b,e). However, for these regions and for temperatures below −50°C, the in situ and model data differ widely. For all regions and where the temperatures are above about −25°C, the CAM5 rates are flat or decrease with increasing temperatures (as a result of missing convective snowfall being treated as rain instead), and the in situ rates are much larger than those from either of the models.

Figure 16 compares the retrieved snowfall rates from 2C-ICE (synthesized from IWCs), 2C-SP retrievals, and GPM Ku-band radar. What is most noticeable from the plots in Fig. 16 is the relatively flat profile of snowfall rates with temperature from both the 2C-SP and GPM retrievals (Fig. 16a), the similarity of the

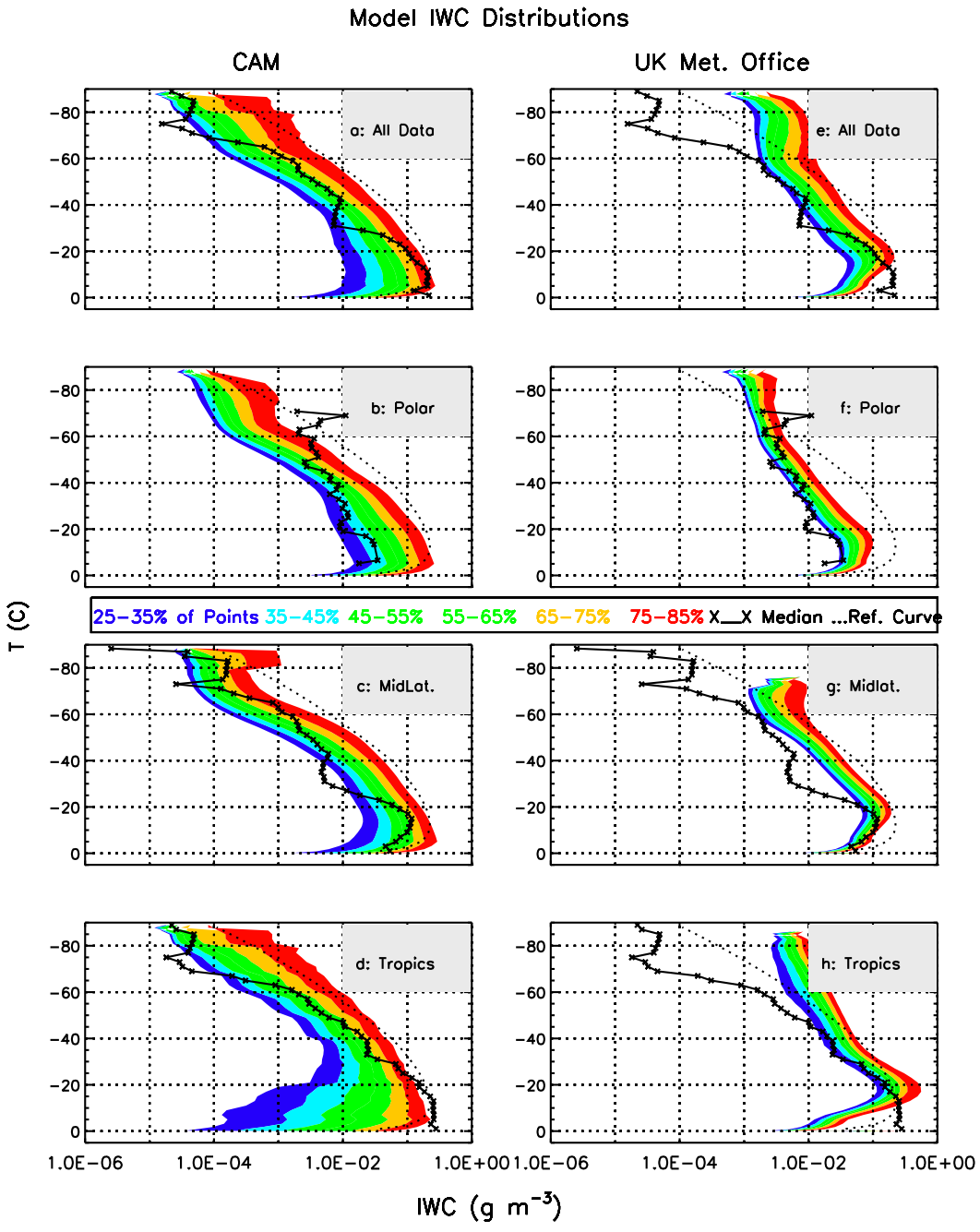

FIG. 10. As in Fig. 9, but for the (left) CAM5 and (right) U.K. model data.

profiles for all regions (Fig. 16b), the apparent effects of the reflectivity detection thresholds used for the 2C-SP retrievals (−15 dB) and GPM (about 13 dB; Toyoshima et al. 2015) on the resulting snowfall rates (Fig. 16c), and the relatively narrow width of the profiles (Fig. 16d). This is most noticeable for the GPM retrievals because of the limitation imposed by the minimum detectable reflectivity. Both the 2C-SP and GPM profiles differ considerably from those derived from both the in situ data and the synthesized 2C-ICE retrievals.

4. Discussion

From the intercomparisons presented in the previous section, this section discusses weaknesses or limitations

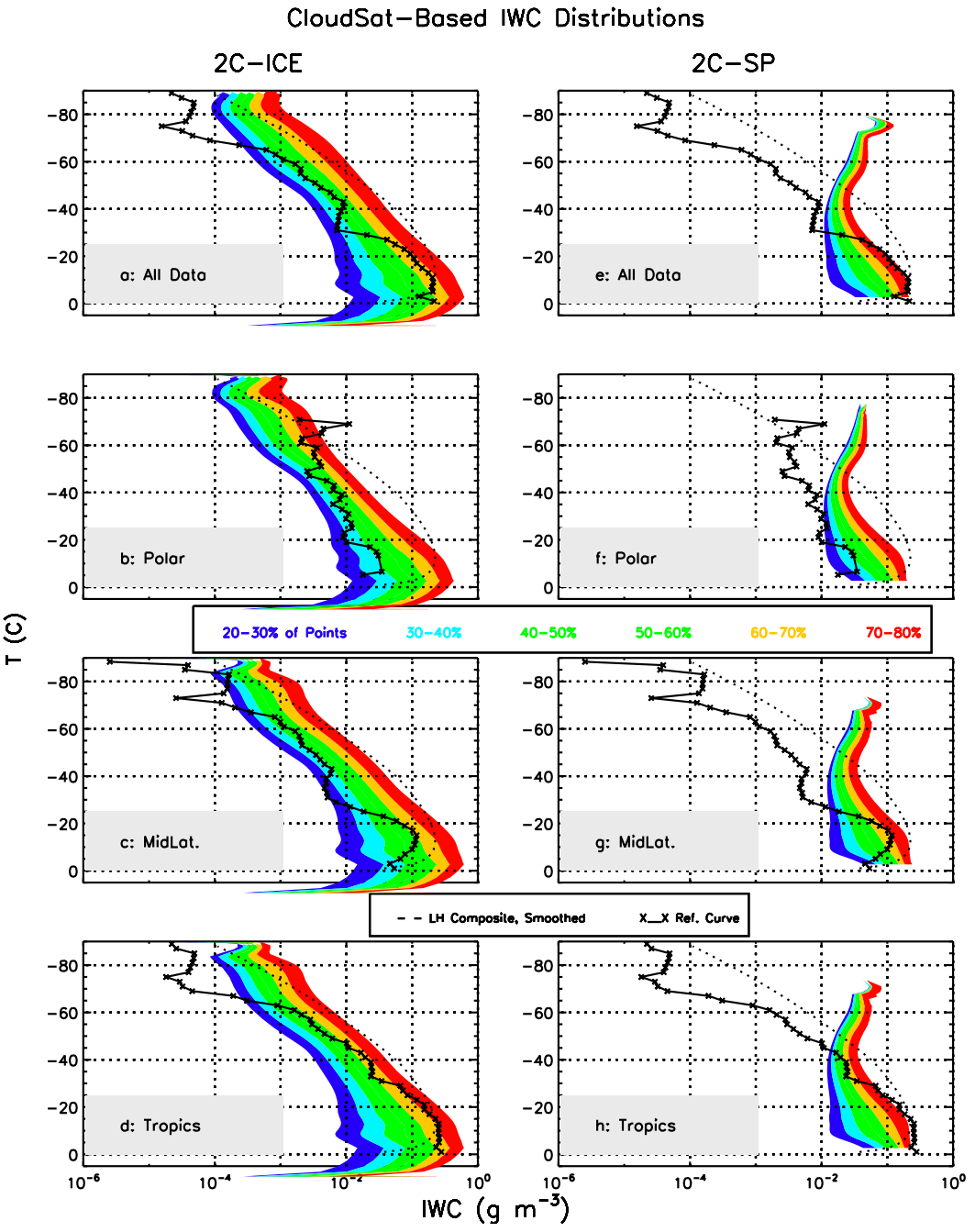

FIG. 11. As in Fig. 9, but for the (left) *CloudSat* 2C-ICE and (right) 2C-SNOW-PROFILE retrievals.

of some of the datasets—SLK, H16, CAM5, UK, 2C-ICE, 2C-SP, and GPM (for snowfall rate). However, given the large differences in the spatial and temporal resolutions of the various data collection methods, it is difficult to definitively draw conclusions on which specific methods are most accurate. Differences between the SLK and H16 dataset are largely due to the primary locations sampled: for SLK, it is the midlatitudes, and for H16, it is primarily tropical locations. Although the combined SLK and H16 dataset has a number of limitations—relatively few measurements for the Arctic and Southern Hemisphere and none for the Antarctic—IWC was directly measured and the dataset does comprise a wide range of temperatures, heights in the atmosphere, and cloud types and conditions. The snowfall rates derived from the

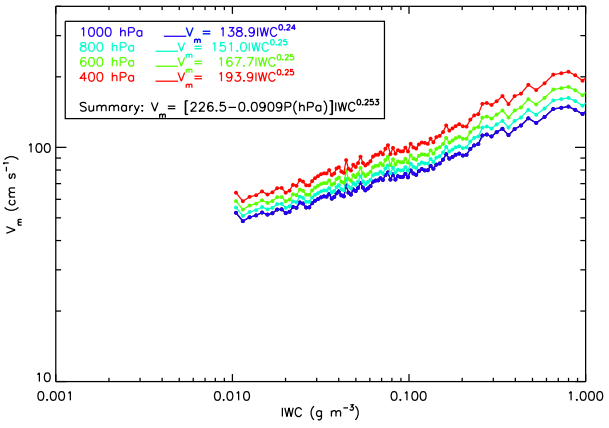

FIG. 12. Mass-weighted fall velocity as a function of the IWC and pressure level. For each PSD in the H16 dataset, snowfall rate and IWC are used to derive a mass-weighted fall velocity from Eq. (1), and then the results for each pressure level are fitted to a power-law curve. A general relationship is then developed across all pressure levels.

combined dataset are also quite reliable given that the input variables of particle mass and cross-sectional areas were either directly measured (from H16) or inferred from it (using SLK). The combined dataset is therefore used here to form the baseline values in this evaluation.

These baseline IWC and S values are constructed by deriving median values of the IWC and S in 2°C increments of temperature from −90° to 0°C for the combined in situ dataset. Likewise, IWC and S were derived in 2°C increments for each of the datasets. Figures 17 and 18 and Table 2 summarize the relationship between the IWC (or S) derived for each method and the baseline values. In Figs. 17 and 18, increasing IWC and S are associated with increasing temperatures, in general. The following points are noteworthy.

- The SLK IWCs conform closely to the SLK–H16 combined in situ dataset (less than a factor of 2, red symbols; Fig. 17a) and begin to deviate from those results at temperatures above about −43°C, where the upper limit of the IWC measurements from the probes used in the SLK studies is reached (see symbol in Fig. 17a). The IWCs from the H16 dataset are under- or overestimated by less than a factor of 2 (red symbols in Fig. 17b), with some overestimates being greater than a factor of 2 at temperatures below about −43°C, largely because of the relatively high detection limit of the probes. The CAM5 IWCs are underestimated throughout (see black symbols below the 1:1 line; Fig. 17c). The U.K. IWCs are also lower than the combined in situ IWCs, except for temperatures below about −63°C, where the IWCs drop off sharply (asterisk in Fig. 17d). The 2C-ICE retrievals are below those of the combined in situ IWCs but are mostly within a factor of 2, except for temperatures below about −68°C, where the IWCs become increasingly overestimated (asterisk in Fig. 17e). The relatively high 2C-ICE IWCs at $T < -68$°C are likely due to the reflectivities being below the detection limit of *CloudSat*, thus necessitating the use of only *CALIPSO* data for the retrievals. The 2C-SP IWCs show an unrealistic trend when temperatures drop below −43°C (asterisk in Fig. 17f), as a result of the reflectivity detection threshold used for the retrievals.
- Trends that are similar to those found for the IWC are noted for the snowfall rate ratios, but the deviations are more significant (Fig. 18). The deviations noted for the GPM dataset are quite extreme (Fig. 18f).
- The IWC and S derived from each method are compared with the combined IWC and S in the form of ratios in Table 2. The mean values found in the 2°C intervals are averaged over 10°C intervals; the results are shown in Table 2, and the right column summarizes the results for all temperatures. Boldface text in Table 2 indicates that the ratio R is $0.5 < R < 2$, while italic text indicates that $R < 0.1$ or $R > 10$. Across all temperatures, the median ratios (first number under "all") and mean ratios (second number under "all") for both in situ datasets are reasonably close to the desired ratio of 1.0, for both the IWC and snowfall rates. The model IWC data are about a factor of 3 or 4 low relative to the combined in situ data across the range of temperatures considered in Table 2, with the exceptions being at the lowest temperatures. Model snowfall rates are considerably lower than the in situ observations, especially so for CAM5. The radar-retrieved IWCs are about a factor of 2 or 3 low relative to the combined in situ data, except for temperatures below −50°C. Ratios that increase with decreasing temperature are clearly noted for the 2C-SP retrievals. With the exception of temperatures below −50°C, snowfall rates derived for the 2C-ICE retrievals compare quite favorably to the combined in situ observations, and those for 2C-SP are quite good for temperatures −50°C and above. The GPM-retrieved snowfall rates show ratios that are close to 1.0 at temperatures of −20°C and above.

A well-defined relationship should exist between S and IWC, with the mass-weighted terminal velocity being the variable that connects them [Eq. (1)]. A better understanding of inconsistencies in the trends noted between S and IWC as a function of temperature for the models (Table 2, cf. ratios in the top and bottom halves of the table) can be identified by comparing the temperature dependence of V_m between the models and in situ observations (Fig. 19).

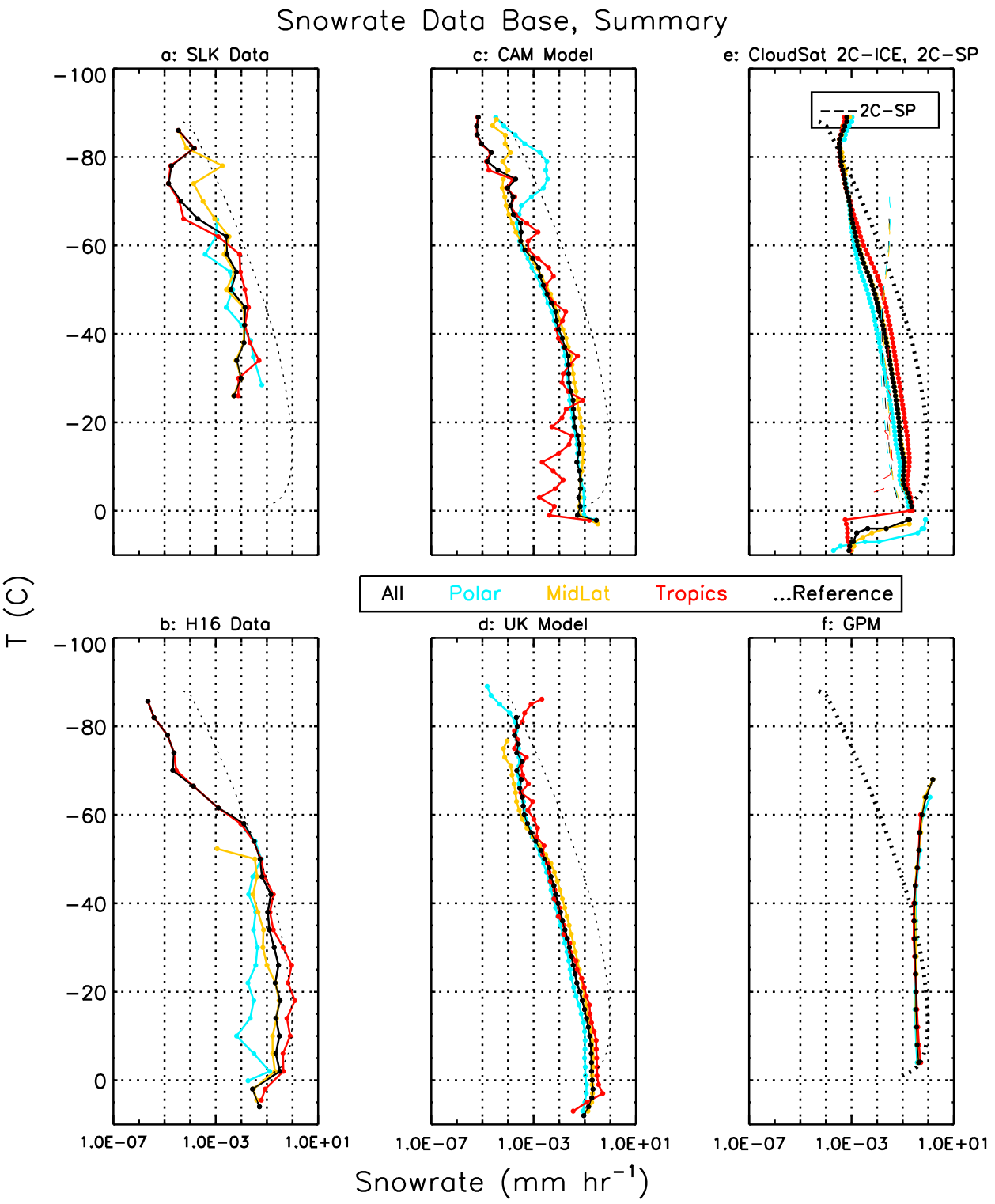

FIG. 13. (a)–(f) As in Fig. 5, but showing the snowfall rate as a function of temperature by research study, where in each panel the plots are for all regions combined and subdivided according to the region.

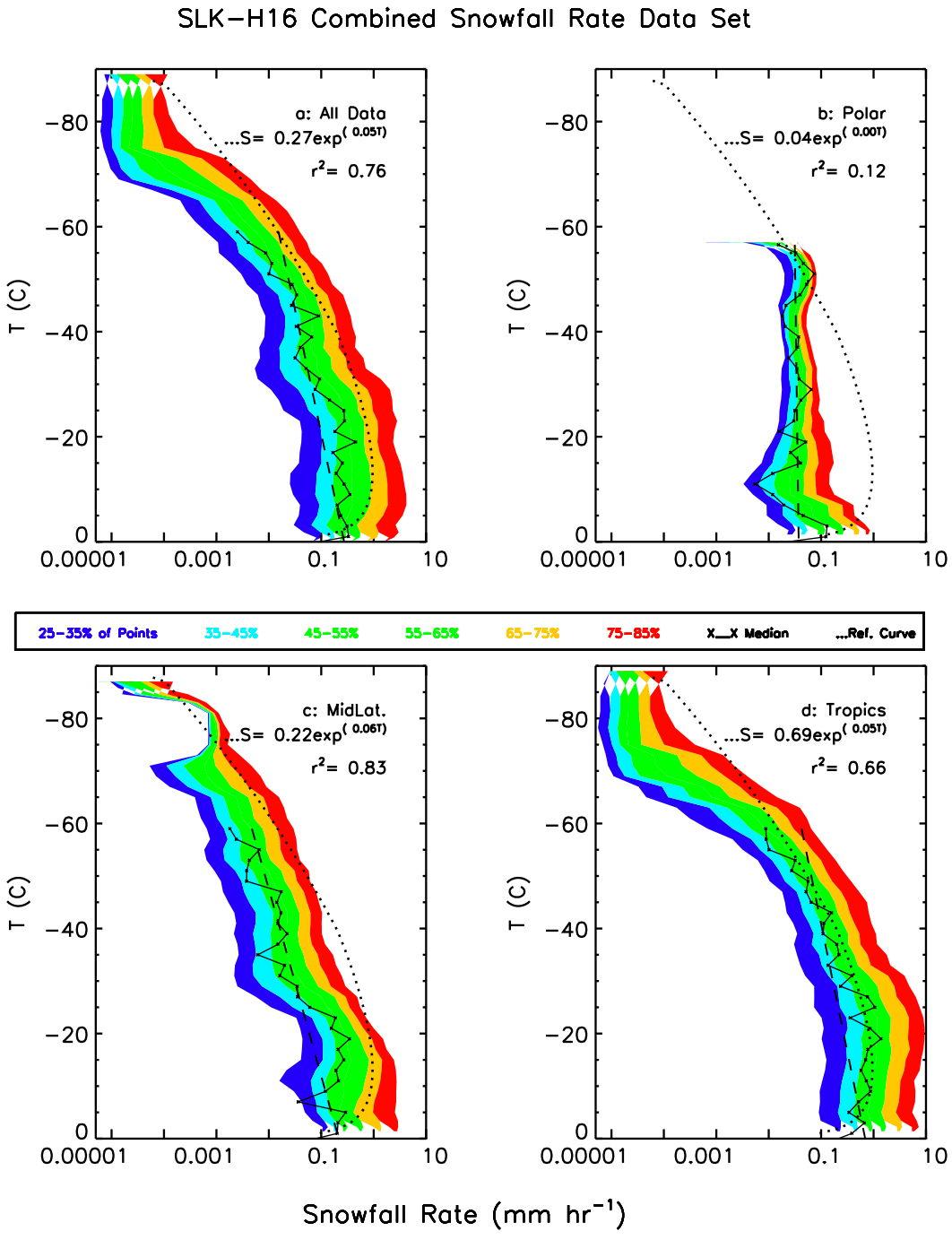

FIG. 14. As in Fig. 9, but for snowfall rates.

Although there is good consistency between the model and observed V_m for the Met Office model (Fig. 19b), the CAM5 model V_m values are nearly constant at temperatures above −60°C (Fig. 19a), which is nonphysical given the expected changes in particle sizes and resulting increases in V_m. This is one reason why the ratios of S and IWC in Table 2 are so distinctly different for the CAM5 values, whereas they are not nearly so different for the U.K. model values.

5. Summary and conclusions

This study has sought to identify the strengths and weaknesses of ice water contents and snowfall rates

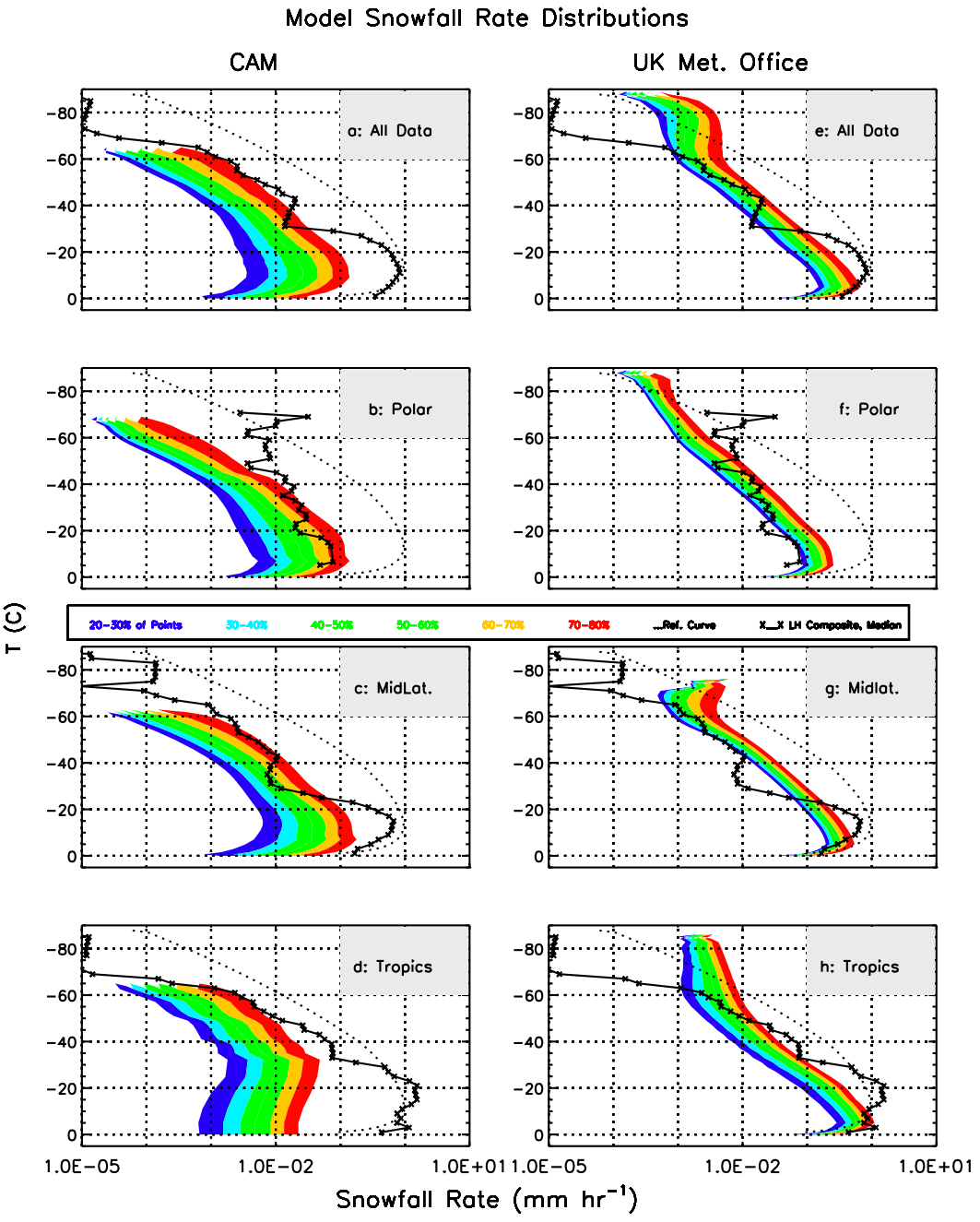

FIG. 15. As in Fig. 10, but for snowfall rates.

obtained using data from research aircraft, climate models, and satellite-borne active remote sensors. The foundation of the analysis is an extensive aircraft-derived database of ice cloud microphysical measurements collected in many geographical areas that cover a wide range of temperatures. Even though the two primary aircraft datasets used in the study included direct measurements of the ice water content, the probes used to collect the data have different measurement ranges, an issue that was considered in the development of a representative in situ database of directly measured IWCs. We also found that consideration of the geographical region rather than whether the precipitating clouds were stratiform or convective was a more meaningful comparison because each region had about the same percentage of clouds classified as one or the other.

Although an increasing number of climate models now use microphysical parameterizations to predict the

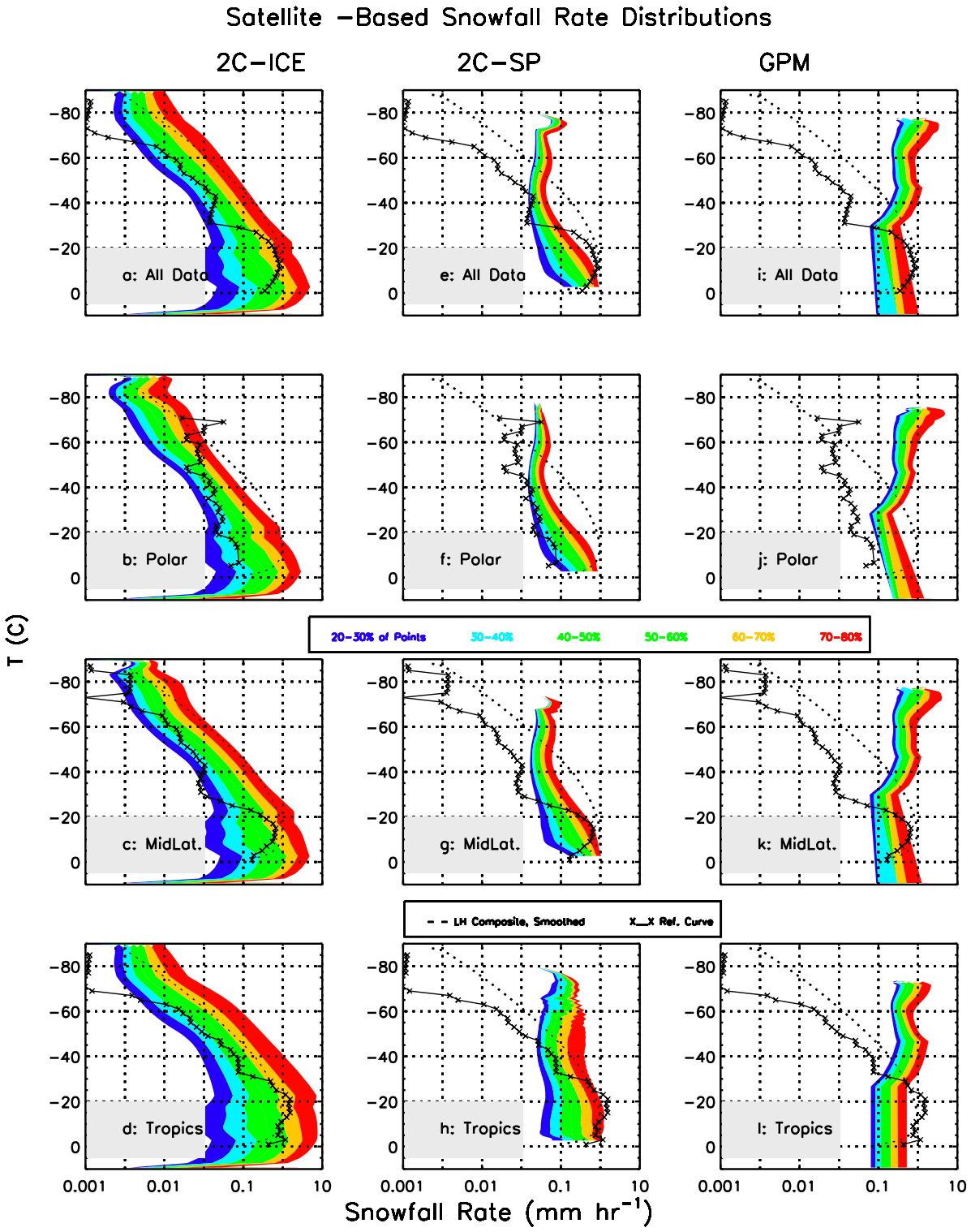

FIG. 16. As in Fig. 11, but for snowfall rates, and with the addition of retrievals from the GPM Ku-band radar.

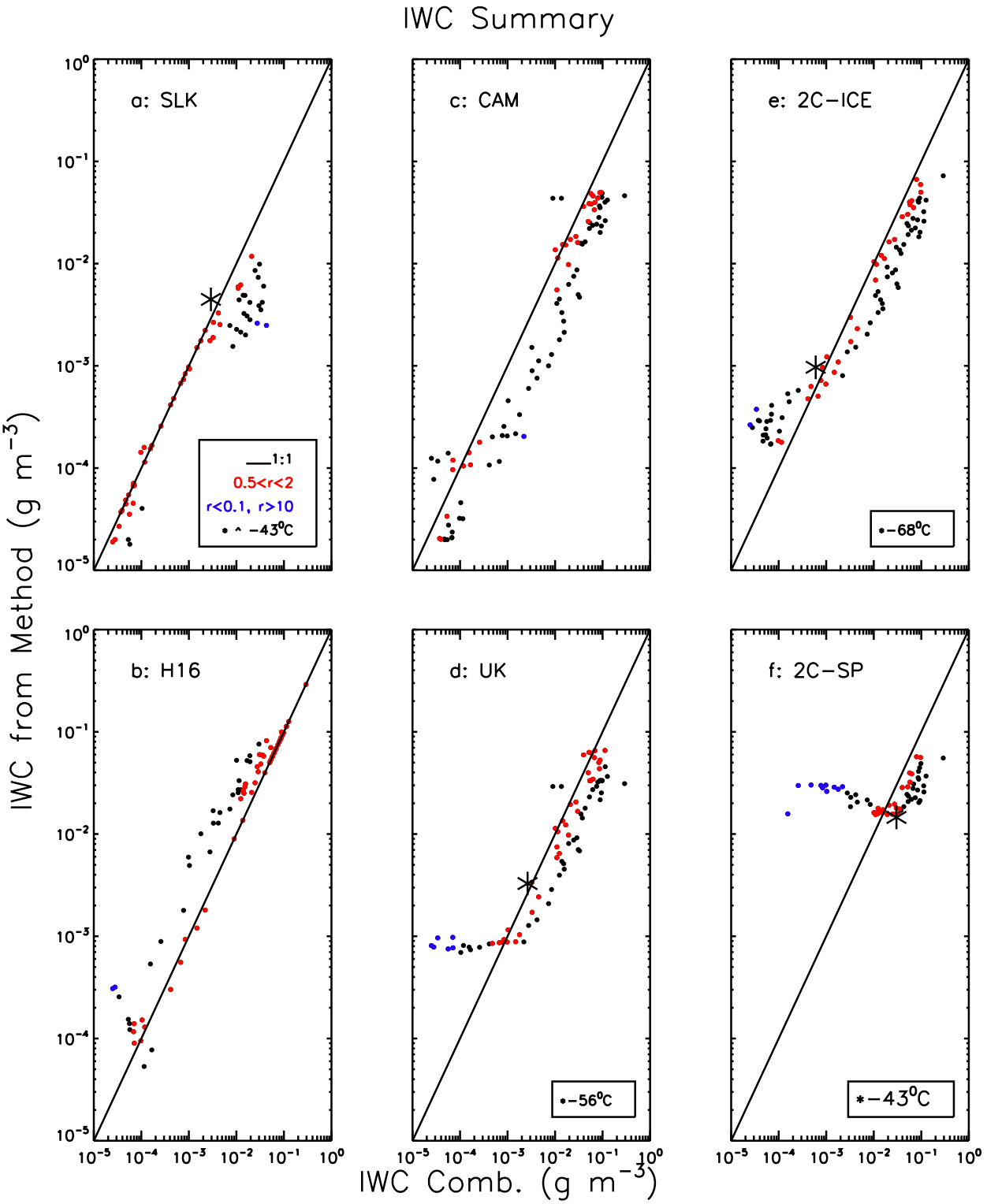

FIG. 17. IWC derived from the combined in situ dataset plotted vs the IWC derived from (a),(b) the individual in situ datasets, (c),(d) models, and (e),(f) retrievals. In (a), *r* refers to the ratio of the median IWC from a given method to the median IWC from the combined in situ dataset.

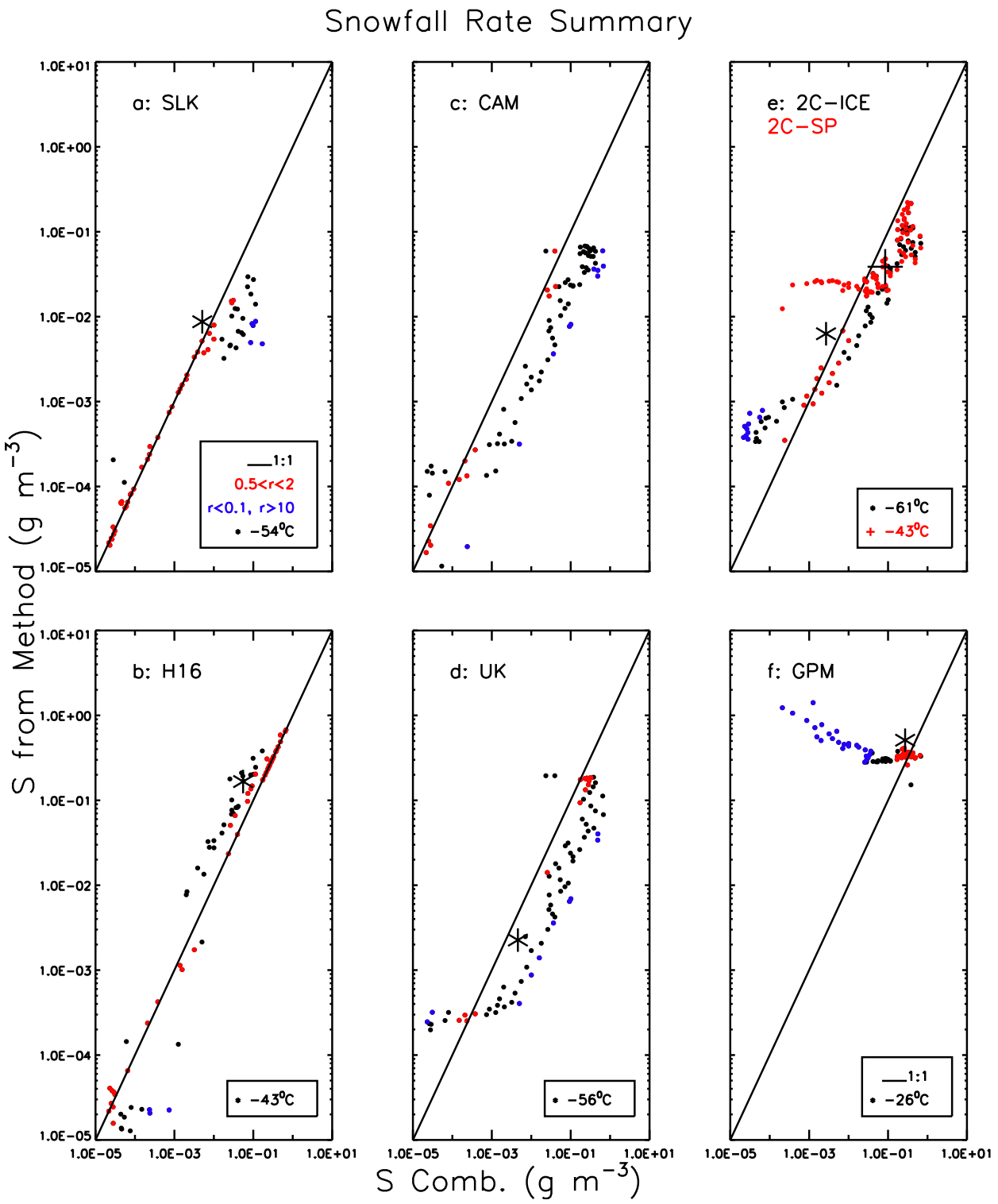

FIG. 18. As in Fig. 17, but for snowfall rates.

TABLE 2. Ratio of IWCs (snowfall rates) to combined in situ IWCs (snowfall rates). Boldface type shows the ratio $0.5 < R < 2.0$ and italic type shows the ratios $R < 10$ and $R > 100$. The ratios $R > 0.5$, $2.0 < R < 100$ are in plain text.

Method	From −90° to −80°C	From −80° to −70°C	From −70° to −60°C	From −60° to −50°C	From −50° to −40°C	From −40° to −30°C	From −30° to −20°C	From −20° to −10°C	From −10° to 0°C	All (median, mean)
					IWC					
SLK	**1.01**	**0.76**	**1.00**	**0.78**	0.32	0.23	*0.10*			**0.63**, **0.63**
H13	**0.97**	2.49	**0.83**	3.6	**1.98**	2.54	**1.12**	**1.00**	**1.00**	**1.47**, 2.17
CAM	0.37	**1.69**	0.27	0.25	0.24	**0.54**	0.42	**0.50**	**0.56**	0.43, **0.67**
UK		*13.9*	1.77	**0.54**	0.39	**0.56**	0.44	**0.83**	0.41	**0.59**, 2.53
2C-ICE	4.35	5.08	**1.15**	**0.53**	0.32	0.49	0.36	0.48	0.47	**0.61**, **1.60**
2C-SP			*30.6*	6.8	**1.17**	**0.83**	0.43	0.42	0.48	**0.72**, 7.98
					Snowfall rate					
SLK	**1.4**	**1.00**	**1.01**	**0.79**	0.31	0.18	*0.06*			**0.92**, **0.81**
H13	0.35	**1.08**	**0.54**	3.34	2.24	3.16	**1.2**	**1.00**	**1.00**	**1.00**, **1.60**
CAM	0.14	2.29	0.23	0.19	0.16	0.28	0.15	0.18	0.26	0.20, **0.54**
UK		7.93	0.40	0.14	0.13	0.24	0.17	0.41	**0.71**	0.30, **1.14**
2C-ICE	7.97	*17.40*	**1.23**	**0.52**	0.31	0.45	0.24	0.31	**0.51**	**0.52**, 3.12
2C-SP			*12.0*	3.01	**0.56**	0.45	0.21	0.31	**0.57**	**0.55**, 4.07
GPM			*1003*	*59.3*	*10.2*	5.22	**1.42**	**1.12**	**1.25**	3.63, *198*

distributions of liquid and ice clouds (Randall et al. 2007), their predictions of ice cloud microphysical properties on a global basis had not been previously evaluated using an extensive in situ database. The comparison of the combined in situ data with the climate model simulations identified anomalies, including too much condensate (ice) fallout in tropical regions and generally too little ice in all regions. The underestimated ice, as suggested from the comparison, is exacerbated for snowfall rates for the following reason. The snowfall rate is approximately proportional to the product of the IWC and mass-weighted terminal velocity V_m, the latter of which from Fig. 12 is approximately proportional to $\mathrm{IWC}^{0.25}$. Thus, an error in IWC can lead to an error of about $\mathrm{IWC}^{1.25}$ for snowfall rates, although the results could be reduced or increased depending on the assumptions the models use for estimating V_m.

Retrievals of ice cloud properties from satellite-borne radars have been evaluated in earlier studies using a limited number of aircraft in situ–satellite collocated data points conducted in limited geographical areas. Our much more extensive, although statistical, comparison suggests that the standard *CloudSat*/*CALIPSO* IWC retrievals are quite reliable for conditions when a combination of radar and lidar data is used for the IWC retrieval. Satellite-based retrievals of snowfall rates from active remote sensors on *CloudSat* perform well at warmer temperatures (warmer than −43°C for *CloudSat* 2C-SP, −20°C for GPM level 2A Ku band), but overestimate expected snowfall rates by increasing the amounts as the temperatures decrease below 0°C.

The increase in the mean snowfall rates with decreasing temperatures noted for the *CloudSat* 2C-SP and GPM retrievals can be explained in the following way. For the 2C-SP retrievals, snowfall rates are only for radar bins in which the reflectivity exceeds about −15.0 dBZ. Likewise, the GPM minimum reflectivity with nonzero snowfall rates is 13.0 dBZ. The average reflectivity for the 2C-SP retrievals for all temperatures from −40° to −80°C varies only from −12.0 to −13.0 dBZ, a result primarily a result of the values straddling close to the minimum reflectivity used for the retrievals. Likewise, the GPM reflectivities throughout the temperature range −40° to −80°C are nearly the same: ~18 ± 2 dB. Because lower temperatures correspond to lower pressures (for both datasets) and the algorithms account for the higher terminal velocities of the ice particles with lower pressures, a relatively constant reflectivity (as with both the 2C-SP and GPM retrievals) yields increasing snowfall rates as pressures decrease. While applicable for detecting near-surface precipitation, thresholds below those used by the algorithms may be more appropriate for precipitation aloft.

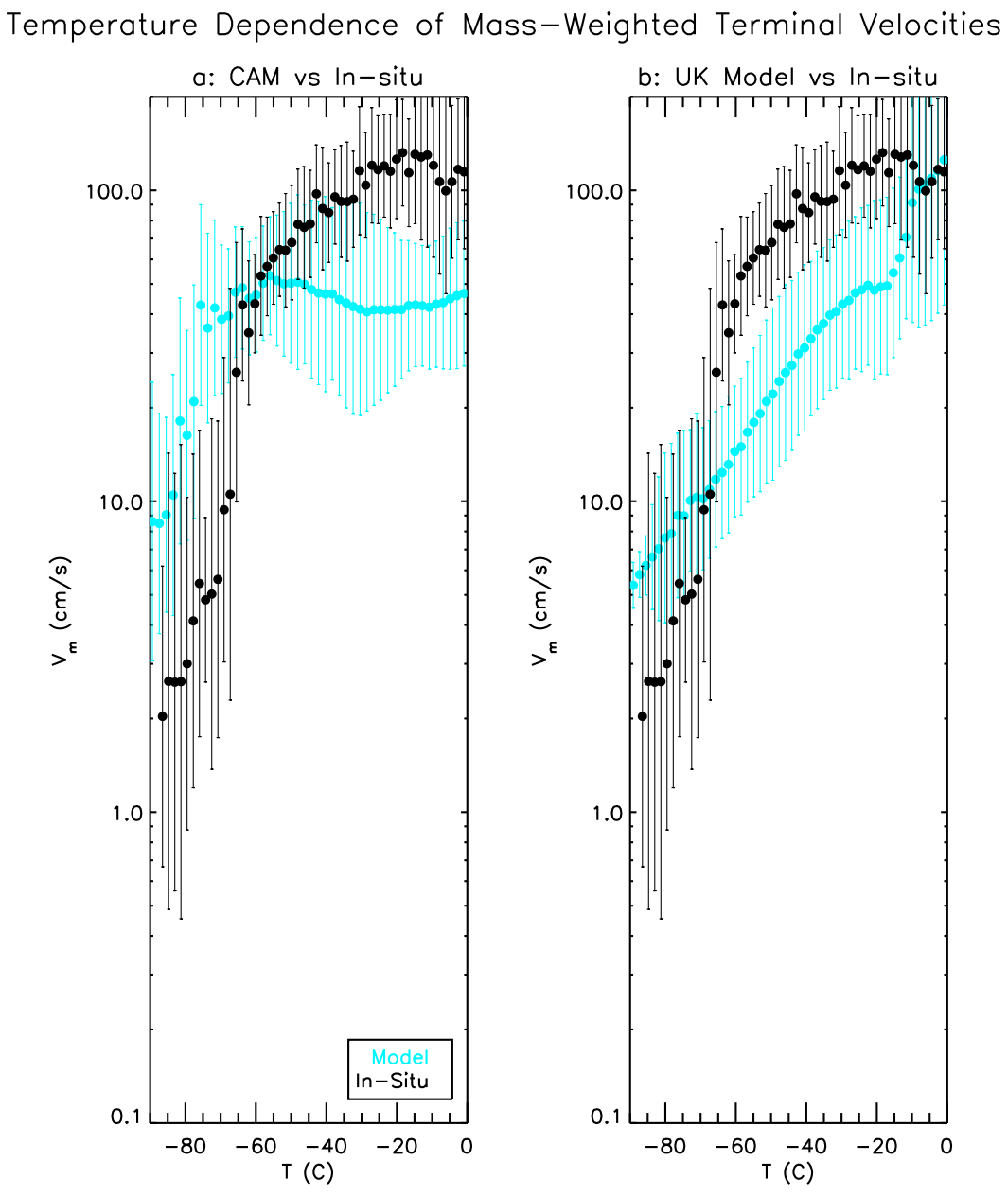

FIG. 19. Temperature dependence of the mean mass-weighted terminal velocity, as derived from the (a) CAM and (b) Met Office models.

It is hoped that this study has elucidated the limitations of the in situ datasets and that it leads to improvements in the representation of ice microphysics in climate models and in the retrievals of ice water content and snowfall rate from satellite active remote sensors. Our study suggests that there is a strong need for more in situ measurements in polar regions and in particular for the Antarctic, where there has not been a comprehensive field program. In the past, climate model simulations have been evaluated based on statistical comparisons between observational datasets and simulated longwave and shortwave radiative properties, cloud fractions, and surface precipitation rates over a global annual cycle (e.g., Pincus et al. 2008). Even if these macroscopic properties are reliably predicted, the cloud ice microphysics may still not be reliably represented. The vertical distribution of the ice microphysics may contribute significantly to the vertical distribution of latent heating and cloud radiation and thus affect the convective and large-scale dynamics. Our dataset

provides the opportunity to improve the representation and retrievals of ice water contents and snowfall rates in cloud through climate models and active remote sensing retrievals.

Acknowledgments. The authors thank Aaron Bansemer for his invaluable help with the in situ dataset. This research was supported by the National Science Foundation and by the Jet Propulsion Laboratory, California Institute of Technology (CA 1451379 Modification 2), which is sponsored by the National Aeronautics and Space Administration. Deb Vane is the *CloudSat* Mission Project Manager. Assistance from Meg Miller for her technical editing of the document was invaluable.

REFERENCES

Bailey, M. P., and J. Hallett, 2012: Ice crystal linear growth rates from −20° to −70°C: Confirmation from wave cloud studies. *J. Atmos. Sci.*, **69**, 390–402, doi:10.1175/JAS-D-11-035.1.

Bretherton, C. S., and S. Park, 2009: A new moist turbulence parameterization in the Community Atmosphere Model. *J. Climate*, **22**, 3422–3448, doi:10.1175/2008JCLI2556.1.

Cao, Q., Y. Hong, S. Chen, J. J. Gourley, J. Zhang, and P. E. Kirstetter, 2014: Snowfall detectability of NASA's *CloudSat*: The first cross-investigation of its 2C-SP product and National Multisensor Mosaic QPE (NMQ) snowfall data. *Prog. Electromagn. Res.*, **148**, 55–61, doi:10.2528/PIER14030405.

Deng, M., G. G. Mace, Z. Wang, and H. Okamato, 2010: Tropical Composition, Cloud and Climate Coupling Experiment validation for cirrus cloud profiling retrieval using *CloudSat* radar and *CALIPSO* lidar. *J. Geophys. Res.*, **115**, D00J15, doi:10.1029/2009JD013104.

——, ——, ——, and R. P. Lawson, 2013: Evaluation of several A-Train ice cloud retrieval products with in situ measurements collected during the SPARTICUS campaign. *J. Appl. Meteor. Climatol.*, **52**, 1014–1030, doi:10.1175/JAMC-D-12-054.1.

——, ——, ——, and E. Berry, 2015: *CloudSat* 2C-ICE product update with a new Z_e parameterization in lidar-only region. *J. Geophys. Res.*, **120**, 12 198–12 208, doi:10.1002/2015JD023600.

Eidhammer, T., H. Morrison, A. Bansemer, A. Gettelman, and A. J. Heymsfield, 2014: Comparison of ice clod properties simulated by the Community Atmosphere Model (CAM5) with in-situ observations. *Atmos. Chem. Phys.*, **14**, 10 103–10 118, doi:10.5194/acp-14-10103-2014.

Field, P., and A. J. Heymsfield, 2015: Importance of snow to global precipitation. *Geophys. Res. Lett.*, **42**, 9512–9520, doi:10.1002/2015GL065497.

Furtado, J. C., J. L. Cohen, A. H. Butler, E. E. Riddle, and A. Kumar, 2015: Eurasian snow cover variability and links to winter climate in the CMIP5 models. *Climate Dyn.*, **45**, 2591–2605, doi:10.1007/s00382-015-2494-4.

Gettelman, A., and H. Morrison, 2015: Advanced two-moment bulk microphysics for global models. Part I: Off-line tests and comparison with other schemes. *J. Climate*, **28**, 1268–1287, doi:10.1175/JCLI-D-14-00102.1.

——, and Coauthors, 2010: Global simulations of ice nucleation and ice supersaturation with an improved cloud scheme in the Community Atmosphere Model. *J. Geophys. Res.*, **115**, D18216, doi:10.1029/2009JD013797.

Gregory, D., and P. R. Rowntree, 1990: A mass flux convection scheme with representation of cloud ensemble characteristics and stability dependent closure. *Mon. Wea. Rev.*, **118**, 1483–1506, doi:10.1175/1520-0493(1990)118<1483:AMFCSW>2.0.CO;2.

Haynes, J. M., T. S. L'Ecuyer, G. L. Stephens, S. D. Miller, C. Mitrescu, N. B. Wood, and S. Tanelli, 2009: Rainfall retrieval over the ocean with spaceborne W band radar. *J. Geophys. Res.*, **114**, D00A22, doi:10.1029/2008JD009973.

Heymsfield, A., and P. Willis, 2014: Cloud conditions favoring secondary ice particle production in tropical maritime convection. *J. Atmos. Sci.*, **71**, 4500–4526, doi:10.1175/JAS-D-14-0093.1.

——, C. Schmitt, and A. Bansemer, 2013: Ice cloud particle size distributions and pressure-dependent terminal velocities from in situ observations at temperatures from 0° to −86°C. *J. Atmos. Sci.*, **70**, 4123–4154, doi:10.1175/JAS-D-12-0124.1.

Hitschfeld, W., and J. Bordan, 1954: Errors inherent in the radar measurement of rainfall at attenuating wavelengths. *J. Meteor.*, **11**, 58–67, doi:10.1175/1520-0469(1954)011<0058:EIITRM>2.0.CO;2.

Hou, A. Y., and Coauthors, 2014: The Global Precipitation Measurement Mission. *Bull. Amer. Meteor. Soc.*, **95**, 701–722, doi:10.1175/BAMS-D-13-00164.1.

Hurrell, J. W., and Coauthors, 2013: The Community Earth System Model: A framework for collaborative research. *Bull. Amer. Meteor. Soc.*, **94**, 1339–1360, doi:10.1175/BAMS-D-12-00121.1.

Iguchi, T., S. Seto, R. Meneghini, N. Yoshida, J. Awaka, T. Kubota, 2010: GPM/DPR Level 2 algorithm reference basis document. Precipitation Processing System, NASA Goddard Space Flight Center, 72 pp. [Available online at http://pps.gsfc.nasa.gov/Documents/ATBD_GPM_DPR_n3_dec15.pdf.]

Khanal, S., and Z. Wang, 2015: Evaluation of the lidar–radar cloud ice water content retrievals using collocated in situ measurements. *J. Appl. Meteor. Climatol.*, **54**, 2087–2097, doi:10.1175/JAMC-D-15-0040.1.

Koop, T., B. Luo, A. Tsias, and T. Peter, 2000: Water activity as the determinant for homogeneous ice nucleation in aqueous solutions. *Nature*, **406**, 611–614, doi:10.1038/35020537.

Krämer, M., and Coauthors, 2016: A microphysics guide to cirrus clouds—Part 1: Cirrus types. *Atmos. Chem. Phys.*, **16**, 3463–3483, doi:10.5194/acp-16-3463-2016.

Liu, G., 2008: A database of microwave single-scattering properties for nonspherical ice particles. *Bull. Amer. Meteor. Soc.*, **89**, 1563–1570, doi:10.1175/2008BAMS2486.1.

Liu, X., and Coauthors, 2012: Toward a minimal representation of aerosols in climate models: Description and evaluation in the Community Atmosphere Model CAM5. *Geosci. Model Dev.*, **5**, 709–739, doi:10.5194/gmd-5-709-2012.

Lock, A. P., A. R. Brown, M. R. Bush, G. M. Martin, and R. N. B. Smith, 2000: A new boundary layer mixing scheme. Part I: Scheme description and single column model tests. *Mon. Wea. Rev.*, **128**, 3187–3199, doi:10.1175/1520-0493(2000)128<3187:ANBLMS>2.0.CO;2.

Luebke, A. E., L. M. Avallone, C. Schiller, J. Meyer, C. Rolf, and M. Krämer, 2013: Ice water content of Arctic, midlatitude, and tropical cirrus—Part 2: Extension of the database and new statistical analysis. *Atmos. Chem. Phys.*, **13**, 6447–6459, doi:10.5194/acp-13-6447-2013.

Morrison, H., and A. Gettelman, 2008: A new two-moment bulk stratiform cloud microphysics scheme in the NCAR

Community Atmosphere Model (CAM5). Part I: Description and numerical tests. *J. Climate*, **21**, 3642–3659, doi:10.1175/2008JCLI2105.1.

Neale, R. B., and Coauthors, 2010: Description of the NCAR Community Atmosphere Model (CAM5.0). NCAR Tech. Note NCAR/TN- 486-STR, 268 pp. [Available online at http://www.cesm.ucar.edu/models/cesm1.0/cam/docs/description/cam5_desc.pdf.]

Norin, L., A. Devasthale, T. S. L'Ecuyer, N. B. Wood, and M. Smalley, 2015: Intercomparison of snowfall estimates derived from the *CloudSat* Cloud Profiling Radar and the ground-based weather radar network over Sweden. *Atmos. Meas. Tech.*, **8**, 5009–5021, doi:10.5194/amt-8-5009-2015.

Park, S., C. S. Bretherton, and P. J. Rasch, 2014: Integrating cloud processes in the Community Atmosphere Model, version 5. *J. Climate*, **27**, 6821–6856, doi:10.1175/JCLI-D-14-00087.1.

Pincus, R., C. P. Batstone, R. J. P. Hofmann, K. E. Taylor, and P. J. Glecker, 2008: Evaluating the present-day simulation of clouds, precipitation, and radiation in climate models. *J. Geophys. Res.*, **113**, D14209, doi:10.1029/2007JD009334.

Protat, A., J. Delanoë, E. O'Connor, and T. L'Ecuyer, 2010: The evaluation of *CloudSat*-derived ice microphysical products using ground-based cloud radar and lidar observations. *J. Atmos. Oceanic Technol.*, **27**, 793–810, doi:10.1175/2009JTECHA1397.1.

Randall, D. A., and Coauthors, 2007: Climate models and their evaluation. *Climate Change 2007: The Physical Science Basis*, S. Solomon et al., Eds., Cambridge University Press, 589–662.

Schiller, C., M. Krämer, A. Afchine, N. Spelten, and N. Sitnikov, 2008: Ice water content in Arctic, midlatitude and tropical cirrus. *J. Geophys. Res.*, **113**, D24208, doi:10.1029/2008JD010342.

Skofronick-Jackson, G., B. Johnson, and S. Munchak, 2013: Detection thresholds of falling snow from satellite-borne active and passive sensors. *IEEE Trans. Geosci. Remote Sens.*, **51**, 4177–4189, doi:10.1109/TGRS.2012.2227763.

Stephens, G. L., and Coauthors, 2002: The *CloudSat* mission and the A-TRAIN: A new dimension to space-based observations of clouds and precipitation. *Bull. Amer. Meteor. Soc.*, **83**, 1771–1790, doi:10.1175/BAMS-83-12-1771.

Toyoshima, K., H. Masunaga, and F. A. Furuzawa, 2015: Early evaluation of Ku- and Ka-band sensitivities for the Global Precipitation Measurement (GPM) Dual-Frequency Precipitation Radar (DPR). *SOLA*, **11**, 14–17, doi:10.2151/sola.2015-004.

Waliser, D. E., J.-L. Li, T. L'Ecuyer, and W.-T. Chen, 2011: The impact of precipitating ice and snow on the radiation balance in global climate models. *Geophys. Res. Lett.*, **38**, L06802, doi:10.1029/2010GL046478.

Wilson, D. R., and S. P. Ballard, 1999: A microphysically based precipitation scheme for the UK meteorological office Unified Model. *Quart. J. Roy. Meteor. Soc.*, **125**, 1607–1636, doi:10.1002/qj.49712555707.

——, A. C. Bushell, A. M. Kerr-Munslow, J. D. Price, and C. J. Morcrette, 2008: A prognostic cloud fraction and condensation scheme. I: Scheme description. *Quart. J. Roy. Meteor. Soc.*, **134**, 2093–2107, doi:10.1002/qj.333.

Wood, N. B., T. L'Ecuyer, D. G. Vane, G. L. Stephens, and P. Partain, 2013: Level 2C snow profile process description and interface control document. Colorado State University Tech. Rep., 21 pp. [Available online at http://www.*CloudSat*.cira.colostate.edu/sites/default/files/products/files/2C-SNOW-PROFILE_PDICD.P_R04.20130210.pdf.]

——, ——, A. J. Heymsfield, G. L. Stephens, D. R. Hudak, and P. Rodriguez, 2014: Estimating snow microphysical properties using collocated multisensory observations. *J. Geophys. Res. Atmos.*, **119**, 8941–8961, doi:10.1002/2013JD021303.